Author Manuscript

Author Manuscript

Author Manuscript

Author Manuscript

HHS Public Access

Author manuscript

Cell Rep. Author manuscript; available in PMC 2021 January 28.

Published in final edited form as:

Cell Rep. 2020 November 17; 33(7): 108398. doi:10.1016/j.celrep.2020.108398.

Tau Pathology Drives Dementia Risk-Associated Gene Networks toward Chronic Inflammatory States and Immunosuppression

Jessica E. Rexach[1], **Damon Polioudakis**[1], **Anna Yin**[1], **Vivek Swarup**[1], **Timothy S. Chang**[1], **Tam Nguyen**[1], **Arjun Sarkar**[1], **Lawrence Chen**[1], **Jerry Huang**[1], **Li-Chun Lin**[3], **William Seeley**[2,3], **John Q. Trojanowski**[4], **Dheeraj Malhotra**[5], **Daniel H. Geschwind**[1,6,7,8,*]

[1]Program in Neurogenetics, Department of Neurology, David Geffen School of Medicine, University of California, Los Angeles, Los Angeles, CA 90095, USA [2]Department of Neurology, Memory and Aging Center, University of California, San Francisco, San Francisco, CA, USA [3]Department of Pathology, University of California, San Francisco, San Francisco, CA, USA [4]Department of Pathology & Laboratory Medicine, University of Pennsylvania, Philadelphia, PA, USA [5]Neuroscience and Rare Diseases, Roche Pharma Research and Early Development, F. Hoffman-LaRoche, Basel, Switzerland [6]Department of Human Genetics, David Geffen School of Medicine, University of California, Los Angeles, Los Angeles, CA 90095, USA [7]Institute of Precision Health, University of California, Los Angeles, Los Angeles, CA 90095, USA [8]Lead Contact

SUMMARY

To understand how neural-immune-associated genes and pathways contribute to neurodegenerative disease pathophysiology, we performed a systematic functional genomic analysis in purified microglia and bulk tissue from mouse and human AD, FTD, and PSP. We uncover a complex temporal trajectory of microglial-immune pathways involving the type 1 interferon response associated with tau pathology in the early stages, followed by later signatures of partial immune suppression and, subsequently, the type 2 interferon response. We find that genetic risk for dementias shows disease-specific patterns of pathway enrichment. We identify drivers of two gene co-expression modules conserved from mouse to human, representing competing arms of microglial-immune activation (NAct) and suppression (NSupp) in neurodegeneration. We validate

This is an open access article under the CC BY-NC-ND license (http://creativecommons.org/licenses/by-nc-nd/4.0/).

*Correspondence: dhg@mednet.ucla.edu.

AUTHOR CONTRIBUTIONS

J.E.R. and D.H.G. designed and supervised the experiments, analyzed and interpreted the results, and wrote the manuscript. J.E.R. completed the experiments, performed the analyses, and generated figures and tables. D.P. performed single nuclear sequencing analysis and differential gene expression on bvFTD and control brain samples. A.Y. performed the iPSC-microglia experiments. J.H. and A.Y. assisted with single nuclear isolation experiments. D.M. contributed to the snRNA-seq study design and sequencing. L.-C.L., W.S., and J.Q.T. curated and provided disease and control brain tissues used for snRNA-seq. V.S. and L.C. contributed to the preparation of raw sequencing data, including QC and normalization, and V.S. provided technical training and supervision of the cWGCNA experiments. T.S.C. contributed exome-based validation of FTD, AD, and PSP module associations. T.N. assisted with image analysis and quantification of the BV2 cell co-culture experiments. A.S. assisted with the BV2 cell co-culture experiments.

SUPPLEMENTAL INFORMATION

Supplemental Information can be found online at https://doi.org/10.1016/j.celrep.2020.108398.

DECLARATION OF INTERESTS

D.H.G. has received research funding from Takeda Pharmaceuticals and Hoffman-LaRoche. D.M. is a full-time employee of F. Hoffmann-La Roche, Basel, Switzerland.

Author Manuscript Author Manuscript Author Manuscript Author Manuscript

our findings by using chemogenetics, experimental perturbation data, and single-cell sequencing in post-mortem brains. Our results refine the understanding of stage- and disease-specific microglial responses, implicate microglial viral defense pathways in dementia pathophysiology, and highlight therapeutic windows.

Graphical Abstract

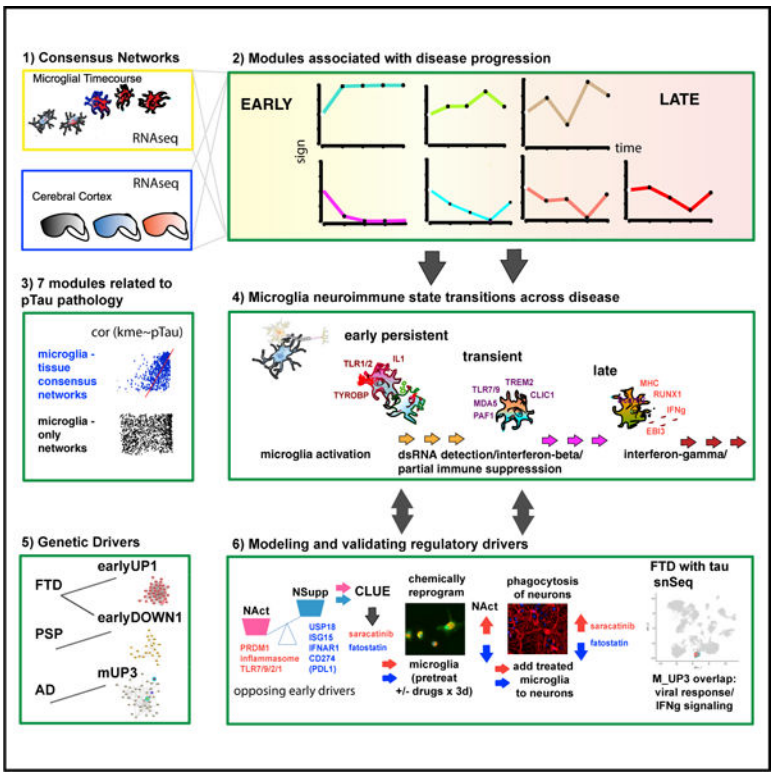

In Brief

Rexach et al. use transcriptional network analysis to define dynamic microglial transitions across neurodegeneration, discovering that three dementias with tau pathology involve dysregulated microglial viral and antiviral pathways. Bio-informatics coupled with experimental validation identifies regulatory drivers, implicating double-stranded RNA and interferon-response genes as drivers of early immune suppression in disease.

INTRODUCTION

Microglia and CNS-resident macrophages are the principal immune cells of the brain, playing critical roles in coordinating the neural-immune response (Hickman et al., 2013). During nervous system injury, microglia can be directly activated by myelin, lipids, or nucleotides released from injured cells to activate pro-inflammatory signaling, such as through the NLRP3 inflammasome complex (Kigerl et al., 2014), and contribute to neuronal dysfunction in multiple ways (Deczkowska et al., 2018; Edwards, 2019; Song and Colonna, 2018). Functional studies in animal models support roles for microglia in the clearance of

Author Manuscript Author Manuscript Author Manuscript Author Manuscript

age-related amyloid beta (Abeta) plaques (Lee et al., 2018) and in the progression of tau pathology and neurodegeneration (Bussian et al., 2018; Kodama et al., 2020; Litvinchuk et al., 2018; Shi et al., 2019). However, microglial responses in neurodegeneration are not monolithic; single-cell genomic studies have begun to delineate substantial heterogeneity among disease-associated microglial states and their trajectories (Grubman et al., 2019; Keren-Shaul et al., 2017; Mathys et al., 2017, 2019). There is a pressing need for biological models to refine our understanding of microglia in human brain disease, including their relationship to specific clinical dementia syndromes and causal genetic factors.

We recently used a systems biology approach to identify a robust, evolutionarily conserved signature of neurodegeneration across humans and multiple mouse models, which is composed of two interconnected neurodegeneration-associated synaptic (NAS) and inflammatory (NAI) modules (Swarup et al., 2019). The NAI module was strongly enriched for markers of astrocytes and microglia. This, coupled with growing evidence that microglial and astrocyte neuroimmune signaling contributes causally to Alzheimer's disease (AD) (Efthymiou and Goate, 2017), suggested that the NAI module would be a powerful starting framework from which to identify early disease-associated microglial changes relevant to human disease. Since our original study was based on bulk tissue RNA sequencing (RNA-seq), downregulated microglial gene expression trajectories were likely obscured by disease-related broad upregulation of microglial markers (De Strooper and Karran, 2016; Swarup et al., 2019). Understanding both upregulated and downregulated signaling pathways within microglia, which likely represent stage and pathology-associated microglial states (Keren-Shaul et al., 2017; Mathys et al., 2017), is necessary to understanding the role of microglia in disease. To achieve this, we reasoned that the integration of cell-type-specific, microglial gene expression data from different stages of disease and control samples with bulk tissue transcriptomes would reveal disease-relevant, cell-specific signaling networks.

Here, we conduct a systematic, integrative analysis of microglial transcriptomic changes that are associated with latent components of neurodegeneration-associated pathways at the tissue level. Our findings parse disease genes into distinct microglial co-expression modules related to progressive stages of neurodegeneration that are robustly modeled in genetically diverse mouse models (n = 492 samples, 14 studies) and conserved in human brain (n = 360, 7 studies). We find that the common genetic risk factors contributing to AD, frontotemporal dementia (FTD)-Pick's disease, and progressive supranuclear palsy (PSP), often referred to as tauopathies because they share the accumulation of pathological tau protein, involves temporally and biologically distinct microglia-associated neuroimmune modules that converge on viral response as a common causal factor. We use multiple data types, integrated across species and human diseases, including chemical genomics experiments, to show that the early microglia disease response reflects a tension between immune suppressors and immune activators. These data and analyses, including proof-of-concept experiments *in vitro* and single nuclear sequencing of the human FTD brain, support a model wherein neuroimmune signaling in tauopathy is dominated by viral response pathways. Initially this involves microglial neuroimmune suppression, driven by type I interferon (IFN) and double-stranded RNA (dsRNA), followed by the activation of type II IFN during the later, frank neurodegenerative phase.

Author Manuscript Author Manuscript Author Manuscript Author Manuscript

RESULTS

Microglial Neurodegeneration-Associated Modules (MNMs) Capture Neuroimmune Interactions Enriched for Microglial Genes and Pathways

We performed consensus weighted gene co-expression analysis (WGCNA; Langfelder and Horvath, 2008; STAR Methods) to combine gene expression data from multiple independent transgenic models expressing human mutant *MAPT*, including sorted, purified microglia at different stages of neurodegeneration (from the rTg4510 model expressing the human P301L MAPT mutation; Wang et al., 2018) and whole-brain tissue (TPR50 model expressing the human P301S MAPT mutation; Swarup et al., 2019) to identify conserved modules of co-expressed genes present in both purified microglia and bulk brain tissue sampled from multiple mouse transgenic lines and genetic backgrounds (Figure 1A; STAR Methods). We identified 13 distinct, robust co-expression modules, including 7 modules enriched for microglial genes, but varying in their relationship to disease, cell type, and temporal trajectories; we call these microglial neurodegeneration-associated modules, MNMs (Figures 1, S1, and S2; Table S1). We compared them with six independent microglia-specific gene expression datasets from transgenic mouse models and humans with AD pathology to identify overlapping patterns of gene expression (Figures 1B, S1C–S1E, and S2F; Table S2), supporting their generalizability. We observed significant overlap between MNMs and disease-associated microglia (DAM), including in their temporal progression (Keren-Shaul et al., 2017), exemplified by a downregulation of homeostatic and upregulation of DAM1 and DAM2 genes (Figure 1B). We note that the microglial modules defined here provide substantially more refinement than the original binary classification. Furthermore, M_UP1 significantly overlaps with a microglial subtype observed in human AD patients (Mathys et al., 2019; Figure 1B).

We capitalized on the sorted, purified microglia, combined with bulk tissue to deconvolute MNM modules into three distinct temporal trajectories with respect to progressive disease stages modeled in the rTg4510 mouse: (1) changing at the earliest disease stage, before neuronal loss, and persistent through later stages (M_UP1, M_DOWN1, M_DOWN2); (2) changing during early periods of neuronal loss and transient (M_UP2, M_DOWN3); and (3) most significantly changing during the late stage of continued neuronal loss and cumulative pathology (M_UP3) (Figure 1C). We also tested whether these co-expression modules were preserved in protein-protein interaction data. We observed significant conservation of protein-protein interactions (PPIs) for all modules (Figure 1D; STAR Methods), further validation of their biological coherence. We next annotated the MNM in detail to uncover disease-associated microglial changes related to the progressive stages of tau-associated neurodegeneration and to identify regulatory drivers of specific microglia disease states and transitions.

We confirmed that the MNMs include expected traits indicative of neuroimmune activity, including: (1) known neuroregulatory pathways, such as complement activation (Schafer et al., 2013), Toll-like receptor (TLR), and interleukin-1β (IL-1β) (Heneka et al., 2013; Figure 1E); (2) strong association with tau pathology, a neuronal driver of neurodegeneration (Figures 1F and S2A); and (3) high overlap with the conserved neuroinflammatory module

Author Manuscript Author Manuscript Author Manuscript Author Manuscript

we identified in our prior study (NAI; Swarup et al., 2019; Figures S2B and S2C). In contrast, when we analyzed WGCNA modules generated using only sorted microglial cell gene expression data from the rTg4510 model, rather than consensus modules based on network edges shared between bulk tissue and the sorted cell data, the correlation with pathological forms of tau was substantially reduced (Figure 1F). Thus, combining bulk tissue and microglial-specific consensus WGCNA identified co-expression patterns that were present in latent forms, but not detected in the analysis of bulk tissue alone. This demonstrates the complementary nature of using both cell-specific and bulk tissue data to resolve neuroimmune-related microglial disease signatures that are closely tied to neuronal pathology.

To explore their preservation across neurodegenerative dementias, we tested module preservation in multiple mouse and human disease datasets (total n = 525 samples from 17 datasets; STAR Methods; Table S2), finding significant preservation in transcriptome data from post-mortem human brain tissue from AD (Allen et al., 2016), FTD (Chen-Plotkin et al., 2008; Swarup et al., 2019), and PSP (Allen et al., 2016) patients (Figure 1G). In addition, all MNMs are preserved in three different transgenic mouse models expressing human *MAPT* mutations (Swarup et al., 2019; Figure S2D) and in microglial-specific datasets from mouse models expressing *PSEN2* (Srinivasan et al., 2016) and *APP* (Wang et al., 2015) mutations, with the exception of M_UP3, which is only weakly preserved in one of the two datasets from mice expressing early AD mutations (Figure S2E). A few modules display variability in their differential expression in different transgenic models, suggesting that they may be conditional on mutational interactions with disease-stage and disease-specific pathology, or possibly by other technical factors distinguishing these mouse models (Figure S2F).

Pathway Analysis to Expand Biological Insights into Microglial Transitions across Disease

The distinct module trajectories suggested that they represented discrete pathways associated with different stages of disease. The time course of the MNMs painted a detailed picture of microglia transitions across disease progression, such that MNMs represented specific biological regulators and pathways, disease genes, immune receptors, and transcription factors (TFs) associated with progressive stages of disease (Figures 1B–1E, 2A, and 2B). M_UP1 represents an early pro-inflammatory response, and the nearly mirror image early M_DOWN1 represents a loss of homeostasis. These are soon followed by the downregulation of cell-cycle and RNA-stabilizing genes represented by M_DOWN2, along with a transient pro-phagocytic response expressed by M_UP2. Finally, we observed an increased expression of genes involved in viral response and type II IFN response represented by M_UP3 (Figures 1E, 2A, 2B, and S2G).

Further examination of the genes within these modules known to regulate immune responses to exogenous signals suggested that gene expression patterns reflected the microglia response to different damage-associated immune activators at different stages of disease progression (Kigerl et al., 2014; Vénéreau et al., 2015; Figure 1E). For example, the earliest upregulated module M_UP1 includes sensors of peptide and lipopeptide immune activators (*Tlr1* and *Tlr2*), whereas the subsequently upregulated module M_UP2 includes sensors of

Author Manuscript Author Manuscript Author Manuscript Author Manuscript

lipid immune activators (*Trem2* and *Scarb2*) and nucleotides (*Tlr7*, *Tlr9*, and *Ifih1*). These nucleotide receptors are known to be activated by viruses or by damaged endogenous DNA or chromatin (Ahmad et al., 2018; Dhir et al., 2018; Dias Junior et al., 2019; Figure 1E). Therefore, this time course analysis suggests that microglia transition from an early response to peptide modulators toward responding to DNA and RNA and expressing genes involved in viral defense over the progression of pathology and neurodegeneration (Figure 2B).

Genetic Risk Factors for FTD, PSP, and AD Converge on Different Viral Response Pathways

We integrated genome-wide common genetic risk using MAGMA (de Leeuw et al., 2015) to determine whether any of the identified MNMs enrich for causal genetic factors. We identified the earliest interconnected MNM genes present in pre-symptomatic disease tissue and called them early MNM sub-modules, reasoning that casual disease pathways should enrich among the earliest MNM components in disease (Figure S3; STAR Methods). We found that the common genetic risk associated with AD, FTD, and PSP (Ferrari et al., 2014a; Höglinger et al., 2011; Lambert et al., 2013) was not randomly distributed, but instead showed distinct patterns of enrichment in each disorder: FTD risk within early_UP1 and early_DOWN1, PSP risk in early_DOWN1, and AD risk in M_UP3 (Figure 3A). We confirmed significant associations using exome array data (Chen et al., 2015), replicating significant associations between AD and M_UP3 ($\beta = 0.19$, $p < 0.001$), FTD and early_UP1 ($\beta = 0.25$, $p < 0.001$), and FTD and early_DOWN1 ($\beta = 0.15$ $p < 0.001$) (Figure S3G). We do not identify the PSP-genome-wide association study (GWAS) association, likely because the exome array dataset is small and therefore relatively underpowered for PSP (Chen et al., 2015; STAR Methods).

We note that the viral response is shared between two of the risk-associated modules (M_UP3 and early_DOWN1) (Figures 3B and 3C). Therefore, human genetic variation contributing to tau-associated dementias involves pathways typically associated with host viral defense. However, in AD, the causal genetic association is with positive regulation of viral defense response (upregulated), whereas in FTD and PSP, the causal association is with viral defense response in a downregulated module (Figures 3B and 3C). Overall, these results show that distinct aspects of microglial biology and viral response pathways are influenced by causal risk in AD versus FTD and PSP. Consistent with these causal relationships defined by genetic enrichment, we were able to demonstrate that the expression of genes involved with viral defense, including the type I IFN response and dsRNA binding, were highly associated with the level of pathological tau phosphorylation in the brains of TPR50 mice (Figures S3H–S3J).

Opposing Neuroimmune Activation and Suppression Modules

We observed that early in disease, microglia upregulate a mixture of signaling receptors and immune response pathways, including viral defense and IFN response genes in two upregulated modules—M_UP1 and M_UP2 (Figures 1 and 2). To further explore the early microglial response in disease, we re-clustered only the genes from M_UP1 and M_UP2 to identify additional co-expression relationships among them (Figure 4A, Module A and Module B; Table S1). This resulted in two new modules upregulated early in disease with

Author Manuscript Author Manuscript Author Manuscript Author Manuscript

nearly identical trajectories (Figure 4B), but demonstrating strongly anti-correlated gene-module connectivity (anti-correlated gene-module connectivity [kME]; Figures 4C and 4D), suggestive of opposing or competing pathways (Langfelder and Horvath, 2008). To test this hypothesis, we leveraged the CMAP database to ask whether large-scale gene perturbations have opposing effects on the trajectories of these two modules (Subramanian et al., 2017). We found that gene overexpression has inverse effects on modules A and B (Figure 4D; 2,161 genes; STAR Methods), which we also confirmed at the levels of gene connectivity (Figure S4A) and PPI (Figure S4B). These patterns were confirmed in 12 independent transcriptome datasets (Figures S4D–S4I), indicating that these two modules represent robust, early microglia responses mediating opposing signaling pathways.

Module A includes protein complexes and pathways of microglial innate neuroimmune activation, including the NLRP3 inflammasome (*Nlrp3*, *Pycard*, *Il1a*, *Il1b*, and *Casp1*) (Ahmed et al., 2017; Ising et al., 2019; Lučiūnaitė et al., 2019), TLRs (*Tlr1*, *Tlr2*, *Tlr7*, and *Tlr9*), and nuclear factor κB (NF-κB) targets (Figures 4E, 4G, and S4A). Since this module represents early microglia innate immune activation in response to extracellular disease-associated signaling molecules (Ahmed et al., 2017), we called it the neuroimmune activation module (NAct). Supporting this interpretation, we found that purified pathological Aβ, an extracellular inducer of pro-inflammatory microglial activity (Lučiūnaitė et al., 2019), stimulates NAct in microglia (Figures 4F and S4C). In contrast, module B includes viral and stress response genes, drivers of immune suppression (*Cd274* [PD-L1], *Il10rb*, *Lag3*, *Usp18*, and *Nfkbia*), and the senescence marker, *Cdkn1a* (Figures 4H and S4A). Therefore, we hypothesized that module B represents microglial neuroimmune suppression and called it the neuroimmune suppression module (NSupp).

We next used the CMAP database to find candidate drivers of NSupp and NAct (STAR Methods), identifying genes that regulate the viral activation of type I IFN among the top drivers of NSupp and suppressors of NAct (*Paf1*; Marazzi et al., 2012; Table S1). Consistent with this, the NSupp module contains both type I IFN receptor genes (*Ifnar1* and *Ifnar2*), the principal downstream TF, *Stat1*, and multiple IFN response activators (*Ifit1*, *Ifit2*, and *Ifit3*) (Figures 4G and 4H). In contrast, the NAct module contains inhibitors of IFN-β production, including *Ifitm3* (Jiang et al., 2018) and *Prdm1* (Doody et al., 2010).

Therefore, we hypothesized that type I IFN is a direct upstream driver of NSupp, which we were able to verify using data from mice treated with *IFNb* (Figure 4I). In contrast, we found that the treatment of mice with IFN-β decreases the microglial expression of NAct (Figure 4I). Because NAct contains no IFN receptor or activators of IFN signaling, our experimental evidence suggested that in microglia, NAct and NSupp appear to represent opposing disease-associated microglial states, likely orchestrated by direct type I IFN activation of NSupp, leading to secondary suppression of NAct.

Type I IFN is a critical driver of immune suppression and tolerance in certain chronic viral infections (Teijaro et al., 2013). Several features of NSupp suggest that in the context of tauopathy it may also represent an immunosuppressive type of IFN-β signaling in disease-associated microglia that are expressing inhibitory immune checkpoint genes (e.g., *Cd274* [PDL-1], *Il10rb*, and *Lag3*) (Snell et al., 2017; Wykes and Lewin, 2018) and inhibitors of

Author Manuscript Author Manuscript Author Manuscript Author Manuscript

immune hyperactivity (e.g., *Usp18*; Basters et al., 2018; Taylor et al., 2018; Figures 4G, 4H, and S4A). Consistent with the model of NSupp activation causing the partial suppression of immune defense, the IFN-induced immune suppressor gene *Usp18* is a NSupp module hub (Figure 5A). Moreover, USP18 modifies protein ISGylation to coordinately regulate multiple genes and pathways in the NSupp module, including *Isg15*, proteostasis, translation, viral response, and exosome formation (Honke et al., 2016; Figure 4H).

Consequentially, these bioinformatic analyses support *Usp18* as a candidate regulator of the integrated biological response represented by NSupp, and therefore we predicted that *Usp18* knockout would disrupt NSupp module connectivity. Remarkably, and consistent with *Usp18* being a critical driver of NSupp (Figure 5A), we found that gene co-expression relationships in NSupp were severely disrupted by *Usp18* knockout. This was despite these animals having a dramatic brain cellular inflammatory response (Goldmann et al., 2015). NAct remains intact in *Usp18* knockout brain, illustrating the specificity of the relationship of *Usp18* to NSupp integrity (Figure 5B) and supporting *Usp18* as a critical driver of the integrated biological response to IFN-β in NSupp. In addition, we find that NAct is highly upregulated in the *Usp18* knockout mouse brain in an IFNAR1-dependent fashion and in *Usp18* knockout primary microglial cultures (Figures 5C and 5D). These data show that the immune suppressor *Usp18* drives the NSupp module, which partially inhibits microglial NAct module gene upregulation in disease, such that when *Usp18* is deleted, NSupp is essentially dissolved, and NAct is de-repressed and up-regulated. These results, summarized in Figure 5H, suggest that the microglial response to IFN-β in disease includes both coordinated changes in cellular function related to viral response (represented by NSupp) and partial suppression of TLR signaling (represented by NAct).

To facilitate proof-of-concept hypothesis testing of our findings, we synthesize the following key observations into a cohesive, testable model (Figure 5H). NAct is activated by extracellular stimuli working through TLR and related receptors (Figures 4E, 4F, S4A, and S4C). NSupp is independently activated by the detection of aberrant intracellular nucleotides leading to type I IFN signaling (Figures 4G–4I) and this NSupp activation secondarily inhibits NAct (Figures 4C, 4D, 5C, and 5D). Genes that drive NSupp inhibit NAct, and vice versa (Figures 4C, 4D, and 4I). This model also describes how NAct and NSupp are functionally interconnected in disease (Figure 5H). NAct is activated initially, representing pro-inflammatory microglia activated by TLR signaling (Figures 4E, 4F, and 5H). As disease progresses, NSupp follows closely due to aberrant nucleotide detection and type I IFN signaling, which in turn partially suppresses NAct. Therefore, the model predicts that the inhibition of NSupp would cause a relative increase in NAct and a net increase in NAct activity, whereas the inhibition of NAct would cause a net decrease in NAct activity.

We experimentally validated a prediction of this model, that NSupp would suppress and NAct would activate microglial neuroimmune activity, using a chemical genomics approach (STAR Methods), identifying 2 compounds predicted to coordinately drive NAct and NSupp module-wide expression. Then, we tested the functional consequences of altering NAct activity using a co-culture of neurons with microglia-like BV2 cells, where BV2 expression of pathways that are highly represented in NAct drives the clearance of neuronal processes in cell culture (Höing et al., 2012; Figures 5E–5G). We found that highdose saracatinib, a

Author Manuscript Author Manuscript Author Manuscript Author Manuscript

Src kinase inhibitor (Wölfl et al., 2013), increases NAct expression and decreases NSupp expression in primary mouse microglial cultures as predicted (Figures 5E and 5F, CMAP score = −90.42 [NSupp] and 36.88 [NAct]). In contrast, we found that fatostatin, a SREBP inhibitor, decreased NAct expression (CMAP score = −90.18 [Nact]), which we confirmed in primary mouse microglial cultures (Figures 5E and 5F). Therefore, we hypothesized that by reducing NSupp, saracatinib would increase the microglial clearance of neuronal process, and by decreasing net NAct activity, fatostatin would decrease the microglial clearance of neuronal processes in cell culture, which is what was observed (Figure 5G). This confirmed predictions that the chemical inhibition of NAct and NSupp has opposing effects on neuroimmune activation and suppression, respectively.

A Model of Early Immunosuppression in Tau-Associated Neurodegeneration

Cumulatively, these unbiased, genome-wide data support a more refined model of early microglial neuroimmune signaling in neurodegenerative disorders with tauopathy (Figures 2B and 5H). At the onset of cellular dysfunction, a pro-inflammatory microglial neuroimmune response, NAct, is activated by extracellular peptide and lipopeptide damage signals. Then, as tau pathology leads to chromatin and nucleotide dysregulation before neuronal loss, nucleotide damage signals activate dsRNA receptors to trigger a microglial type I IFN response that drives the expression of NSupp pathways involved in stress response, exosome, and viral entry (Figure 4H), while suppressing the specific microglial immune attack pathways represented by NAct, including the NLRP3 inflammasome and TLR1 and −2 signaling (Figures 4E and S4A). This results in reactive microglia that suppress pathways early in disease that are related to pathogen clearance consistent with the known immunosuppressive role of IFN-β elsewhere (Snell et al., 2017). As disease progresses to include frank neurodegeneration, microglia undergo additional dynamic states, including increased type II IFN signaling, exogenous antigen presentation, T cell regulation, and cell death (Figures 1E, 2A, 2B, and S2G). Importantly, this model suggests that tau pathology may contribute to the inhibition of microglial immune clearance activity early in disease, causing a state of relative immunosuppression, which may lead to disease progression.

We tested this model with a proof-of-concept validation experiment in human microglia, asking whether type I IFN can functionally inhibit NAct. We pre-treated human-induced pluripotent stem cell (iPSC)-derived microglia (Haenseler et al., 2017; STAR Methods) with IFN-β and tested the ability of fibrillar Aβ, a NAct activator (Figures 4F and S4C), to induce the secretion of IL-1β, a prominent member of the NAct pathway in these human cells (Figures 4E and 4G). We observed that Aβ increased IL-1β secretion in untreated microglial cultures and that IFN-β treatment significantly suppressed Aβ-induced IL-1β secretion in human iPSC-induced microglial cultures (Figure 5I).

Validation by Single Nuclear Sequencing of Human Disease Tissue

Having annotated and functionally validated the NSupp and NAct modules, we levered them as biomarkers to measure microglial neuroimmune activity in human post-mortem disease samples. We found that NSupp upregulation is a consistent feature seen in the brain tissue of subjects with AD and PSP (Figure 5J), and in single-cell data from AD (Figure 5K),

Author Manuscript Author Manuscript Author Manuscript Author Manuscript

suggesting that microglial NAct suppression may be a shared feature of the chronic phases of these two tau-associated dementia syndromes.

Another prediction based on the mouse microglia module trajectory analysis (Figure 2) is a delayed, biphasic type II IFN response with early suppression and late increase (M_DOWN1, M_UP3; Figures 1C, 1E, 2A, 2B, and S2G). To validate the relevance of these findings to humans, we performed deep single-cell sequencing in human post-mortem brain from dementia patients and controls to determine the microglia changes associated with tau pathology. We performed single nuclear sequencing of 107,620 nuclei from pre-central gyrus from patients having behavioral variant FTD (bvFTD) with tau immunoreactive inclusions (Pick's disease) and matched controls, identifying 2,891 microglial nuclei for this analysis after quality control (QC), clustering and cluster annotation (Figure 6A). Remarkably, we observed concordance between disease-associated signaling pathways represented in M_UP3 and microglia from patients with FTD-Pick's; in particular in type II IFN, a specific activator of M_UP3 (Figures 2A, 2B, 6C, and S2G). Significantly upregulated in bvFTD microglia are genes that can stimulate IFN-γ production (*IL18*, *LILRB1*, *TLR7*, and *SPP1*) (Renkl et al., 2005) and genes that mediate IFN-γ response (*IFNGR1*, *IRF8*, *B2M*, and *JAK2*; Figures 6C, 6D, and S5E). Gene Ontology (GO) and PPI analyses demonstrate additional pathway-level alignment between M_UP3 and bvFTD microglia, including antigen presentation, IFN-γ signaling, and regulation of cell death (Figure 6C), further confirming that the latent microglia disease states that we identified in mice are relevant to human disease.

DISCUSSION

Through an integrative systems-biology approach, we have identified microglia neuroimmune networks related to early stages of neurodegeneration modeled in mice harboring mutant tau protein. Combining bulk tissue and cell-type-specific data from multiple divergent transgenic mice and human single-cell data, we identified seven conserved microglia modules that were also represented in post-mortem tissue from patients and controls. By integrating data from brain tissue with sorted cell data, we achieved a unique perspective on neuroinflammatory signaling in neurodegeneration that we show neither bulk tissue nor single-cell-type data can achieve on its own. The seven microglial co-expression modules identified represent a refined, more integrative, and complementary view of microglial neuroimmune trajectories representing distinct signaling and neuroimmune states in neurodegeneration.

Our refined analyses of microglia-associated changes at different stages of tauopathy suggest that early immune activation is accompanied by immune suppression, likely driven by the activation of IFN-β, and we provide multiple analyses supporting this model. Recent experimental data show that IFN receptor blockade reduces sustained microgliosis and synaptic clearance (Roy et al., 2020), and IFN treatment inhibits microglial phagocytosis (Mudò et al., 2019) and release of pro-inflammatory cytokines (Moore et al., 2020). Here, we provide complementary evidence that IFN-β may also suppress genes involved in microglial immune clearance (NAct; including *Il1b*, *CD74*, *IL27ra*, *B2m*, *Fcer1g*, *Cd14*, *Ptprc*, *Tlr2*, *Trem2*, *Cd68*, and *Cxcr4*) and drive genes that function in early immune

Author Manuscript Author Manuscript Author Manuscript Author Manuscript

suppression (NSupp; *PD-L1*, *Isg15*, *Tgfbr2*, *Usp18*, and *Zc3h12a*; Mao et al., 2017). At later disease stages, microglia transition to expressing chronic viral response pathways, together with pathways that were relatively quiescent or downregulated at earlier stages, such as the type II IFN response.

Several endogenous stimuli are capable of activating type I IFN in disease (Cuellar et al., 2017; Dhir et al., 2018), but our observations suggest that pathological tau may trigger the IFN pathway through cytosolic dsRNA detection. We find that both dsRNA detection and IFN pathways are highly correlated with pathological tau burden in brain (Figures S3H–S3J) and both the cytosolic dsRNA receptor *Ifih1* (MDA5) and RIG1 pathway are hubs of the NSupp module (Figure 4H). This is particularly salient based upon the recent observation that pathological tau drives chromatin destabilization (Guo et al., 2018; Sun et al., 2018), a known source of endogenous dsRNA that can activate *Ifih1* (MDA5) and trigger an IFN response outside of the CNS (Ahmad et al., 2018; Cuellar et al., 2017). These intracellular events contrast with extracellular tau seeds and fibrils, which experimental evidence suggests activate microglia NAct pathways (Pampuscenko et al., 2020; Stancu et al., 2019).

These data suggest a parsimonious model wherein dsRNA, released following chromatin destabilization in injured neurons and/or other cells in response to tau pathology, activates early suppressive pathways driven by type I IFN (NSupp) to suppress acute microglia defense pathways that would clear infection (NAct). These observations predict that the inhibition of NSupp, either through blockade of dsRNA, IFNAR1 pathways, or immune checkpoints, would reduce early immune dysregulation triggered by pathological tau and, at least in part, restore microglia damage response and promote viral clearance mechanisms. Our model also predicts that without this suppression, disease pathology may drive immune hyperactivity and cellular injury.

These data fit with recent observations that IFN-driven microglial immunosuppression in aging may also contribute to age-related susceptibility to neurodegeneration (Deczkowska et al., 2017). In addition, our observation that AD, FTD, and PSP susceptibility genes converge on viral response pathways is consistent with the notion that the microglial type I IFN response may influence early disease progression, including the propagation of tau pathology (Ising et al., 2019; Stancu et al., 2019). These observations suggest an important causal connection between viral defense and pathological tau, with interactions varying over the course of disease.

From this perspective, different stages of dementia are associated with different forms or levels of immune activation. These analyses suggest that early immune suppression and delayed viral response, rather than immune activation alone, may contribute to disease progression and promote chronic inflammation as disease progresses into its clinical phase, particularly in response to tauopathy. Future functional and mechanistic studies will be needed to experimentally test and extend this model, which has significant implications for the development and timing of therapeutic interventions targeted at the neuroimmune response.

Author Manuscript Author Manuscript Author Manuscript Author Manuscript

STAR★METHODS

RESOURCE AVAILABILITY

Lead Contact—Further information and requests for resources and reagents should be directed to and will be fulfilled by the Lead Contact, Professor Daniel H. Geschwind (dhg@mednet.ucla.edu).

Materials Availability—This study did not generate new unique reagents.

Data and Code Availability—RNaseq data of mice microglia cultures treated with fatostatin and saracatinib are available at the NCBI Gene Expression Omnibus (GEO) database under accession number GEO: GSE146866.

FTD-tau and control snSeq data are available from dbGAP under accession number dbGAP: phs002197.v1.p1

Custom code used for the analysis is available on github: https://github.com/dhglab/Tau-pathology-drives-dementia-risk-associated-gene-networks-towards-chronic-inflammatory-states-and

EXPERIMENTAL MODEL AND SUBJECT DETAILS

Human Subjects—Frozen brain tissue (precentral gyrus) were obtained from the UCSF Neurodegenerative Disease Brain Bank and University of Pennsylvania Center for Neurodegenerative Disease Research Brain Bank. We obtained samples from 16 total individuals, including 8 subjects with clinical diagnosis of behavior variant frontotemporal dementia and neuropathological diagnosis of Pick's disease (Tau protein pathology) and controls (n = 8). Samples were balanced age (mean: 68 years old -Pick's, 66 years old - control), PMI (mean: 15.98 hours – Pick's, 12.78 hours - control) and tissue RNA integrity number (RIN; mean: 6.1 -Pick's, 5.6 -controls) (Table S2). Samples were obtained with informed consent and institutional IRB approval for each brain bank. IRB exemption was obtained from the UCLA IRB to authorize use of de-identified human postmortem brain single nuclear sequencing data in this study. Neuropathological diagnosis was verified by Professor William Seeley at UCSF.

Cell Lines—The induced pluripotent stem cells (iPSC) line #1205 (a de-identified, human control line; Sloan et al., 2018) was provided by the lab of professor Sergiu Pasca (Stanford University); and obtained with informed consent and institutional IRB approval by the Pasca lab. Use of this line in the Geschwind lab is approved by the UCLA Embryonic Stem Cell Research Oversight (ESCRO) Committee. The iPSC line was checked when thawed and confirmed for expression of markers of pluripotency (OCT4, SSEA4). For line maintenance and quality control, the line was tested to confirm negative mycoplasma contamination, and checked for chromosomal copy number changes using comparative genomic hybridization array. CO_2 was tightly controlled. iPSC cell morphology was visually inspected to ensure against spontaneous differentiation. For cell cultures, iPSCs were plated on 5μg/mL Vitronectin (Thermo Fisher, A14700) coated plates in Essential 8 (E8) media (Thermo Fisher, A1517001). Cells were maintained with daily media changes and kept at 37°C and

Author Manuscript Author Manuscript Author Manuscript Author Manuscript

5% CO_2. Cells were passaged approximately every 4 days or at 60%–70% confluency using 0.5mM EDTA/DPBS for 3 minutes at RT. EDTA/DPBS was aspirated and cells were blown off by gently using 1mL of media. iPSCs were passaged as small cellular clusters at a 1:10 dilution to help proliferation.

iPSC derived microglia-like cells were generated and validated as previously described (Haenseler et al., 2017). Embryoid bodies (EBs) were made by adding 3×10^6 iPSCs to each Aggrewell-800 well (24-well plate; StemCell Technologies, 34850) in 2mL of E8 media supplemented with 50ng/mL BMP-4 (Peprotech, 120-05ET), 50ng/mL VEGF (Biolegend, 583702), and 20ng/mL SCF (Peprotech, 300-07). ROCK inhibitor Y-27632 was added to the media only on day 0. For days 1–4, media was replaced by performing two-half changes daily. On day 5, EBs were gently collected with wide-boar pipette tips and transferred to T-75 flasks with 12mL of MacPre media. EBs were maintained in macrophage precursor (MacPre) media, consisting of AIM-V media (Thermo Fisher, 12055083) supplemented with 100U/mL penicillin/streptomycin, 0.055ɛM beta-mercaptoethanol (Life Technologies, 31350–010), 100ng/mL M-CSF (Biolegend, 574806), 25ng/mL IL-3 (Biolegend, 578006), and 2mM GlutaMAX (Thermo Fisher, 35050–061). EBs seeded in T-75 flasks were cultured at 37°C and 5% CO_2 for 7–12 days before performing weekly media changes to ensure EBs attached to the flask. Macrophage precursor cells were released from EBs into the media approximately 3–4 weeks post-seeding of EBs into flasks. At that point, the supernatant was collected weekly and passed through a 40mm cell strainer. Supernatant was spun down at 500xg for 5 minutes to pellet cells. Macrophage precursor cells were resuspended in microglia media to differentiate cells toward a microglia-like state and plated on non-treated tissue culture plates. Human 1205 iPSC-derived microglia cells were maintained in RPMI media (Thermo Fisher, 11875093) supplemented with 2mM GlutaMAX, 100U/mL penicillin/streptomycin, 0.055mM beta-mercaptoethanol, 1x N2 supplement (Thermo Fisher, 17502048), 100ng/mL IL-34 (Biolegend, 577906), and 10ng/mL GM-CSF (Biolegend, 766104). Microglia-like cells can be maintained up to 14 days after initial plating with media changes every 3–4 days.

BV2 female C57BL/6 mouse microglia cultures (RRID: CVCL_0182) were passaged at 70%–80% confluency weekly. 0.25% Trypsin/EDTA was used to dissociate cells and spun down at 1000rpm for 5 minutes to pellet the cells. Supernatant was aspirated and cells were resuspended and passaged at 1:10 on 6-well plates for maintenance with complete media. Cells were kept in 37°C with 5% CO_2 in DMEM media (Thermo Fisher, 11995065) supplemented with 5% heat-inactivated fetal bovine serum (HI-FBS) and 1% Penicillin/Streptomycin. Media was replaced every 3–4 days.

Primary Cell Cultures—Mouse primary embryonic cortical neurons were prepared from E15 C57BL/6J embryos. Briefly, cortical tissue from day 15 (E15) C57BL/6J embryos was collected, dissected and washed in ice-cold Hank’s balanced salt solution (HBSS; Thermo Fisher, 14175095). Tissue was incubated in 0.25% trypsin (Invitrogen) in the presence of DNase I (Roche, 4536282001) at 37°C for 10 minutes. Tissue was washed with cold HBSS and titurated in plating media (Neurobasal Medium; Thermo Fisher Scientific, 10888–022), 10% heat-inactivated fetal bovine serum (Thermo Fisher Scientific, 16140071), 25mM sucrose and 0.25% GlutaMAX (Thermo Fisher, 35050–061) in the presence of DNase I.

Author Manuscript Author Manuscript Author Manuscript Author Manuscript

Dissociated cells were centrifuged at 125xg for 5 minutes at 4°C, resuspended in culture medium, counted and plated in poly-D-lysine coated and etched glass coverslips. Neurons were cultured in Neurobasal Medium supplemented with 2% B27 (17504-044), 2mM GlutaMAX and penicillin/streptomycin (100 U/mL). BV2-neuronal co-cultures were also maintained in this neuronal culture media.

Mouse primary embryonic microglial cultures were prepared from P1 C57BL/6J pups as previously described (Saura et al., 2003). This protocol has two steps – first the culturing of mixed glia followed by isolation of microglia. Cortical tissues were collected in 0.1% glucose/PBS. Meninges and blood vessels were removed and brains were transferred to 6mL of 0.05% trypsin/PBS (Invitrogen) and pipetted through P1000 tip one time to gently mince. Tissue was incubated for 20 minutes at 37°C and transferred to 50mL conical tube containing 25mL of DMEM-F12 (Thermo Fisher, 1132003) supplemented with 10% heat-inactivated fetal bovine serum (HI-FBS; Thermo Fisher). Tissue settled to bottom of tube, and the media was replaced with fresh 30mL of DMEM-F12 (Thermo Fisher) + 10% HI-FBS. Samples were titurated until completed homogenized and aliquoted (at 1/2 brain per plate) into 150mm Petri dish containing 30mL DMEM-F12 + 10% HI-FBS. After two days, and then every 5 days, the media was replaced. After 20 days in culture, microglia were isolated as follows: cell plates were agitated 15 minutes at 150–200rpm on an orbital shaker. Media containing floating microglia was collected in a 50mL conical tube. Plates were washed three times in PBS. To remove astrocytes, cells were covered in 9mL of 0.25% Trypsin/HBSS (14175095) diluted 1:3 in serum free DMEM-F12 and incubated at 37°C for 30 minutes until astrocytes floated off the plate. Media containing astrocytes was aspirated and cells washed 3x with 10mL of PBS. Subsequently, adherent microglia were removed by incubating in 5mL of 0.25% Trypsin/HBSS for 3 minutes at 37°C. Microglia were then collected in 5mL of DMEM-F12 + 10% HI-FBS, spun down, and resuspended in 5mL culture media (DMEM-F12 supplemented with 2% HI-FBS, penicillin/streptomycin (100U/mL) and 50μM beta-mercaptoethanol) for 24 hours prior to drug treatment. Microglia purity was assessed by immunocytochemistry.

METHOD DETAILS

Dataset Acquisition and Filtering—Both RNaseq datasets used as input for consensus WGCNA were previously generated. The TPR50 dataset (Swarup et al., 2019) includes gene expression data from frontal cortex dissected from male mice expressing P301S *MAPT* or WT controls (TPR50 transgenic model (Onishi et al., 2014)) in three different genetic backgrounds (C57BL6/J, F1 C57BL6/J x DAB, F1 C57BL6/J x FVB), and includes samples collected at 3 months of age (n = 6 per group) and 6 months of age (n = 5–6 per group). The rTg4510 microglia dataset includes gene expression data obtained from microglia purified using C11b FACS collected from mice expressing P301L *MAPT* and WT controls (rTg4510 transgenic model (Santacruz et al., 2005)), pooled to include microglia from 8–10 forebrains per sample, with n = 4 replicate samples per time points (2, 4, 6, and 8 months of age) (AMP-AD Knowledge Portal: https://doi.org/10.7303/syn2580853) (Wang et al., 2018). Data were filtered for low read counts (> 80% of the sample with > 10 reads with HTSeq quantification) and normalized using log2-transformation and linear regression prior to use for consensus WGCNA and module expression trajectory analysis, as previously described

Author Manuscript Author Manuscript Author Manuscript Author Manuscript

(Swarup et al., 2019). The rTg4510 transgenic mouse is a model of neurodegeneration secondary to human mutant *MAPT* and additional factors (Gamache et al., 2019).

Additional publicly available datasets were used throughout the study for validation or comparison (Table S2; and Key Resources Table). Mouse datasets consist of microarray or RNaseq transcriptomics data from a variety of transgenic mice models –PS19 (Swarup et al., 2019), rTg4510 and JNPL3 (AMP-AD Knowledge Portal, available on Synapse: https://www.synapse.org), PS2APP (Srinivasan et al., 2016), USP18 knockout (Goldmann et al., 2015), IFNAR knockout (Goldmann et al., 2015), 5xFAD (Wang et al., 2015), CK-p25 (Mathys et al., 2017), and *in vitro* and *in vivo* treatments – Abeta42 (Johansson et al., 2015; Woodling et al., 2014), IFN-beta-expressing AAV (Deczkowska et al., 2017), and IFN-gamma (Rock et al., 2005). Human postmortem data consist of AD temporal cortex (Allen et al., 2016), FTD frontal cortex, and PSP temporal cortex (Allen et al., 2016), as well as single nuclear sequencing data from Alzheimer's and control prefrontal (Mathys et al., 2019) and entorhinal cortex (Grubman et al., 2019). IRB exemption was obtained from the UCLA IRB to authorize use of de-identified human postmortem sequencing data in this study.

Microarray or RNaseq datasets downloaded from the Gene Expression Omnibus (GEO) were read into R and processed as follows. Microarray data were log2-transformed and normalized by quantile normalization. Gene counts were filtered to remove low read counts (> 80% of the sample with > 10 reads with HTSeq quantification), corrected for guanine-cytosine content, gene length and library size, and log2-transformed using the CQN package in R (Hansen et al., 2012). The resulting data was used as an input to test module preservation, average gene expression and/or eigengene expression.

mRNA Weighted Co-expression Network Analysis—In order to identify gene co-expression networks present both in purified microglia and frontal cortical brain tissue, and across multiple transgenic mouse strains and genetic backgrounds, we utilized consensus WGCNA as previously described (Swarup et al., 2019) using the WGCNA R package (Langfelder and Horvath, 2008), applied to the TPR50 dataset of forebrain RNaseq from mice aged 6 months, and the Tg4510 dataset of purified microglia described above. The input data were generated from (1) microglia purified from P301L *MAPT* and WT mice from the Tg4510 model (Santacruz et al., 2005) at ages 2, 4, 6 and 8 months (n = 4 mice per condition) (AMP-AD Knowledge Portal: https://doi.org/10.7303/syn2580853) (Wang et al., 2018), and (2) frontal cortex from P301S *MAPT* and WT mice from the TPR50 model with three different genetic backgrounds (C57BL6/J, F1 C57BL6/J x DAB, F1 C57BL6/J x FVB) at 6 months of age (n = 5–6 per group), a period with extensive gliosis and neuronal Tau pathology but prior to frank atrophy (Swarup et al., 2019).

Similarity matrices were created using the Consensus WGCNA method as previously described (Li and Horvath, 2007). In the signed network, the similarity between genes reflects the sign of the correlation of their expression profiles. The signed similarity matrix was then raised to power β to emphasize strong correlations and reduce the emphasis of weak correlations on an exponential scale. A thresholding power of 14 was chosen (as it was the smallest threshold that resulted in a scale-free R2 fit of 0.8) and the consensus network was created using the function blockwiseConsensusModules() to calculate the component-

Author Manuscript Author Manuscript Author Manuscript Author Manuscript

wise minimum values for topologic overlap (TOM), with parameters set as networkType = "signed," deepSplit = 2, detectcutHeight = 0.995, consensusQuantile = 0.0, minModulesize = 100, mergeCutHeight = 0.2. Using 1 — TOM (dissTOM) as the distance measure, genes were hierarchically clustered. The resulting modules or groups of co-expressed genes were used to calculate module eigengenes (MEs; or the 1st principal component of the module). Gene – module eigengene connectivity score (kME, was calculated using the WGCNA function consensusKME() with parameters set to consensusQuantile = 0.20, signed = TRUE. Modules were annotated using the GOElite package (Zambon et al., 2012). We performed module preservation analysis using consensus module definitions (Langfelder et al., 2011). MEs were correlated with transgenic condition to find disease-associated modules. Module hubs were defined by calculating module membership (kME) values which are the Pearson correlations between each gene and each ME. Gene expression was correlated with pT231 Tau levels measured by ELISA to calculate the "gene significance" relationship with pT231 Tau, as defined by the WGCNA method (Langfelder and Horvath, 2008), using gene expression data from the TPR50 model (6 months, n = 36), and this was further correlated (Pearson's) with kME to assess the relationship between pT231 Tau and gene-module connectivity. All network plots were constructed using the Cytoscape software (Saito et al., 2012). Module definitions from the network analysis were used to create synthetic eigengenes from which to calculate the expression trajectory of various modules in different gene expression datasets.

Clustering of Gene Subsets—To apply gene co-expression methods to understand co-expression relationships among subsets of module genes in either the original consensus dataset, or in the TPR50 dataset of pre-symptomatic mice at 3 month of age, we again used the WGCNA package (Langfelder and Horvath, 2008). Biweighted mid-correlations were calculated for a subset of genes from selected consensus modules to create an adjacency matrix that was further transformed into a topological overlap matrix (with TOMType = "unsigned"). Using 1 — TOM (dissTOM) as the distance measure, genes were hierarchically clustered using the following parameters (deepSplit = 2, detectcutHeight = 0.999, minModulesize = 40, dthresh = 0.1, softPower = 7). The resulting modules, or groups of co-expressed genes, were used to calculate module eigengenes (MEs; or the 1st principal component of the module). The significance of intramodular connectivity was assessed for each module using a permutation test (10,000 permutations), and all modules were confirmed to have permuted p value < 0.001. "Early submodules," described in Figures 3 and S3, were derived by re-clustering M_UP1 and M_UP2 genes to generate "earlyUP" modules, or M_DOWN1, M_DOWN2 and M_DOWN3 genes to generate "earlyDOWN" modules, using the 3 month of age frontal cortex TPR50 gene expression data (Swarup et al., 2019). "NSupp and NAct," described in Figures 4 and 5, were derived from re-clustering the M_UP1 and M_UP2 genes, keeping only genes with annotated PPI in either Bio-grid (Stark et al., 2006) or Inweb databases (Rossin et al., 2011), using the same gene expression data used for the consensus WGCNA analysis (purified microglia from the Tg4510 model and frontal cortex TPR50 dataset (6 months of age)).

Module Preservation Analysis—We used module preservation analysis (Langfelder et al., 2011) to validate co-expression in independent mouse and human datasets. Module

Author Manuscript Author Manuscript Author Manuscript Author Manuscript

definitions from consensus network analysis were used as reference and the analysis was used to calculate the Zsummary statistic for each module. This measure combines module density and intramodular connectivity metrics to give a composite statistic where Z > 2 suggests moderate preservation and Z > 10 suggests high preservation (Langfelder et al., 2011).

Module Gene Set Enrichment Analysis—Gene set enrichment analysis was performed using a two-sided Fisher exact test with 95% confidence intervals calculated according to the R function fisher.test(). We used p values from this two-sided approach for the one-sided test (which is equivalent to the hypergeometric p-value) as we do not assume *a priori* enrichment (Rivals et al., 2007). To reduce false positives, we used FDR adjusted p values (Benjamini and Hochberg, 1995) for multiple hypergeometric test comparisons. For cell-type enrichment analysis we used published mouse brain dataset (Zhang et al., 2014). The test background for over-representation analyses was chosen as total genes input into the consensus analysis (overlap of genes expressed in Tg4510 microglia and TPR50 frontal cortex RNaseq datasets).

To test module enrichment for single cell microglial gene expression signatures, we used signatures defined from publicly available single-cell studies pertaining to microglia and/or neurodegenerative disease (Hammond et al., 2019; Keren-Shaul et al., 2017; Mathys et al., 2017; Olah et al., 2018; Scott et al., 2018). Specifically, for disease-associated microglia (Keren-Shaul et al., 2017; Mathys et al., 2017), we set cluster signatures to be the top 100 differentially expressed genes between two microglia clusters, as defined in their corresponding publications. For microglial and macrophage clusters defined from young and aged mouse brain in (Hammond et al., 2019), we defined clusters signatures as published except duplicated genes were removed among the young cluster group (C1, C2a, C2b, C3, C4, C5, C6, C7a, C7b, C7c, C8, C9, mono_macA, mono_macB), and aged cluster group (aging_C1a, aging_C1b, aging_C2, aging_C3, aging_C4) to increase the distinctiveness of each cluster. To define genesets from the single-cell microglial trends from injured mouse brain published in (Hammond et al., 2019), we used the genes with fold change > 1.5 in control versus injured, and injured versus control mice, respectively, to define the injury_C1 and injury_C2 genesets. For human microglial gene clusters defined in (Olah et al., 2018), we defined cluster signatures as genes with expression fold > 1.8 compared to any other clusters. For human Alzheimer's disease brain single cell signatures (Grubman et al., 2019; Mathys et al., 2019), we defined differentially expressed genes as those with FDR < 0.05 and logFC > 0.1 using the published differential gene expression data.

Gene Set Annotation—Genes in network modules were characterized using GO-Elite (version 1.2.5), using as background the set of input genes used to generated the modules being annotated (Zambon et al., 2012). GO-Elite uses a Z-score approximation of the hypergeometric distribution to assess term enrichment, and removes redundant GO or KEGG terms to give a concise output. We used 10,000 permutations and required at least 3 genes to be enriched in a given pathway at a Z score of at least 2. We report only biological process and molecular function category output.

Author Manuscript Author Manuscript Author Manuscript Author Manuscript

Protein-Protein Interaction Analysis—To assess and visualize protein-protein interactions among module genes, we used STRING (version 10.5; (Szklarczyk et al., 2017) with the following setting (organism: *Mus musculus* for mouse data, and *Homo sapiens* for human data; meaning of network edges: confidence; active interaction sources: experiments and databases; minimal required interaction score: medium confidence (0.400), max number of interactors to show: none). Data was exported and visualized using the Cytoscape software (Saito et al., 2012).

Transcription Factor Binding Site Enrichment Analysis—Transcription Factor Binding Site (TFBS) enrichment analysis using an in-house package that incorporates TFBS as previously described (Chandran et al., 2016). Briefly, this published code uses TFBS position weight matrices (PWMs) from JASPAR and TRANSFAC databases (Matys et al., 2003; Portales-Casamar et al., 2010) to examine the enrichment for TFBS within each module using the Clover algorithm (Frith et al., 2004). To compute the enrichment analysis, we utilized three different background datasets (1000 bp sequences upstream of all mouse genes, mouse CpG islands, and mouse chromosome 20 sequence).

Connectivity Map (CMAP) Analysis—For a given module, the top 150 module genes (ranked by kME) were used as input for the QUERY app in the Broad's CMAP database, version CLUE (Subramanian et al., 2017). This signature was used to query 7,494 gene overexpression or knockdown experiments carried out across 9 cell lines for similar (positive connectivity score) or opposite (negative connectivity score) effects on gene expression signatures, incorporating Kolmogorov-Smirnov statistics (a nonparametric, rank-based pattern-matching strategy) as described (Lamb et al., 2006; Subramanian et al., 2017). Per the CMAP website (https://clue.io), for each module-perturbagen pair, the connectivity score (*tau*) is a standardized percentile score that compares the similarity of the query geneset to the perturbagen compared to all other reference genesets in CMAP; such that 95 indicates that 5% of reference genesets show stronger connectivity to the perturbagen than the query dataset. For our analysis, we used the mean "connectivity scores" which is calculated from the combining data generated independently in 9 cell lines (see Table S1).

MAGMA—Summary statistics for genome-wide association studies for AD (Lambert et al., 2013), PSP (Höglinger et al., 2011) and FTD (Ferrari et al., 2014a) were used as an input for MAGMA (v1.06) (de Leeuw et al., 2015) for gene annotation to map SNPs onto genes (with annotate window = 20,20) and the competitive gene set analysis was performed to test module associations with GWAS variants (permutations = 100,000). All genes assigned to a given module were used as the input for each module. Consensus modules and re-clustered modules were run as separate groups in MAGMA given that they contain overlapping genes. Additional FDR correction was applied across all the competitive p value outputs from MAGMA for all modules used in the study.

Exome-based Validation of MAGMA—Summary statistics from Alzheimer's disease, frontotemporal dementia and progressive supranuclear palsy exome array analyses were downloaded from (Chen et al., 2015). To incorporate protein-protein interaction, summary statistics were used as input to the network burden test, NetSig (Horn et al., 2018). NetSig

Author Manuscript Author Manuscript Author Manuscript Author Manuscript

determines a gene's network association with disease. Generalized least-squares regression was used to determine if NetSig results were enriched in gene modules. Regression covariates included gene length and mean protein expression, including the log of these values. To account for linkage disequilibrium, error was correlated for genes within 5 megabase pairs.

Drug Treatments—Saracatinib (S1006) and fatostatin (F8932) were purchased from Selleckchem and Sigma. Primary microglia were treated with saracatinib (1 μM, 24h), fatotastatin (1 μM, 72h) or corresponding DMSO vehicle control as indicated. BV2 cells were pretreated with saracatinib (1 μM, 72h), fatotastatin (1 μM, 72h) or DMSO vehicle control (equal volume as drug, 72h) in BV2 cell culture media. Pre-treated BV2 cells were dissociated using trypsin/EDTA, washed and resuspended in neuronal culture media, counted, and plated on top of mouse primary neuronal cultures (aged 14 days *in vitro*) at a ratio of 1 BV2 cell: 3 neurons. BV2 cell-neuronal co-cultures were treated with drug or DMSO vehicle control for three days in neuronal culture media (Neurobasal medium (Thermo Fisher) supplemented with 2% B27 (17504-044), 2 mM GlutaMAX Supplement (Thermo Fisher) and penicillin/streptomycin (100 U/mL)).

iPSC-induced microglia cultures were plated on black 96-well clear bottom plates (Corning, 3603) and maintained in RPMI media (Thermo Fisher, cat no 11875085) supplemented with 100ng/mL IL-34 (Biolegend, 577906) and 10ng/mL GM-CSF (Biolegend, 766404) for 10 days prior to experimentation. Human iPSC-induced microglia and were then treated in culture media with 1uM fibrillar amyloid beta for 6 hours at 37°C and 5% CO2 with or without pretreatment of 20ng/mL recombinant human interferon beta (IFN-β; R&D Systems, cat no. 8499-IF) for 2 hours.

Cell Staining and Quantification—Following BV2-neuronal coculture, cells were fixed in 4% paraformaldehyde, permeabilized for 20 minutes in 0.25% Tween-20, and immunostained with a microglial marker rabbit anti-Iba1 (1:1000, Wako, 019-19741), and guinea pig anti-synaptophysin (1:1000; Synaptic Systems) for 2 hours at room temperature, followed by secondary antibodies (donkey anti-rabbit 488 (1:500; Invitrogen, A21206); goat anti-guinea pig 555 (1:500; Invitrogen, A21435) for one hour at room temperature. After washing the slides with Tris-buffered saline with Tween-20 (TBST), slides were stained with DAPI (4′,6-diamidino-2-phenylindole, a blue-fluorescent DNA *stain*). Cells were imaged at 20x using Zeiss Axioplan II microscope with six representative images captured and quantified per coverslip in a blinded fashion. The local density of neuronal processes surrounding BV2 cells was quantified in ImageJ by measuring the synaptophysin staining density within the BV2 cell and surrounding area (defined by BV2 nuclei (DAPI) area and adjacent area extending out from the DAPI image perimeter using the ImageJ function "Mask of Image Points" (version 1.1) with settings "add mask points within distance" = 1 micron. We used the expanded DAPI area to localize BV2 cells rather than the Iba1 signal because Iba1 staining intensity varied from cell to cell.

RNA sequencing—RNA was isolated from primary mouse microglia using NucleoSpin RNA Plus (Takara, 740984.50) and RNA sequencing libraries were prepared using the QuantSeq 3′ end labeling kit (Lexogen, 015.96) according to the manufacturer's protocol,

Author Manuscript Author Manuscript Author Manuscript Author Manuscript

and sequenced on a HiSeq4000 to 50M single end reads (1 × 65bp). Reads were aligned against GRCm38 using STAR (Dobin et al., 2013). Transcripts were quantified and annotated against GencodeM11 using Rsubread (Liao et al., 2019). Sample QC was performed using network connectivity from the WGCNA package (Langfelder and Horvath, 2008) and z-score relative to the mean gene PCA, excluding samples that were > 3 standard deviations. Samples were normalized with CQN (Hansen et al., 2012). Sequencing batch correction, when needed, was performed using ComBat (Johnson et al., 2007).

ELISA—Total tau and pT231 tau contents were measured by commercial tau ELISA kits according to the manufacturer's instructions (total tau - KHB0041; pT231 tau - KHB8051, Invitrogen), as previously described (Swarup et al., 2019). Mouse IL-1beta was quantified using cell culture supernatant via ELISA (R&D Systems, DY401) according to the manufacturer's protocol, with absorbance measured at 450nm.

Single Nuclear Sequencing (snRNaseq)—Nuclei were prepared from 60–70mg of frozen brain tissue per sample, with all procedures carried out on ice or at 4°C with RNase-free reagents. Briefly, postmortem frozen brain tissue was lysed in 3mL homogenization buffer (250mM sucrose, 150mM KCl, 30mM $MgCl_2$, 60mM Tris, 0.1% v/v Triton X-100, 1μM DTT, supplemented with 0.2U/mL RNase Inhibitor (NEB, M0314), Complete protease inhibitor cocktail (Roche, 11697498001)) using a Wheaton Dounce Tissue Grinder (30 strokes with pestle B). The lysate was filtered through a 40μm cell strainer and centrifuged at 1000xg for 8 minutes to obtain a nuclear pellet. To remove debris, the nuclear pellet was resuspended in 350μL homogenization buffer and 1:1 with an equal volume of 50% iodixanol buffer (Iodixanol 60% v/v combined with buffer of 250 mM sucrose, 150mM KCl, 3mM $MgCl_2$, 60mM Tris), then layered over 600μL of 29% iodixanol buffer (Iodixanol 29% v/v combined with buffer of 250mM sucrose, 150mM KCl, 3mM $MgCl_2$, 60mM Tris) and centrifuged at 13500xg for 20 minutes. The supernatant was discarded, and nuclei gently resuspended and washed in 1mL of 1% BSA/PBS. The nuclei were visually inspected to confirm complete lysis and nuclear integrity. Nuclei were manually counted and diluted to a concentration of 1000 nuclei/μL in 1% BSA/PBS. For single-nucleus RNA sequencing (snRNA-seq), libraries were prepared using the Chromium Single Cell 3' Reagent Kits v2 according to the manufacturer's protocol (10X Genomics, 1000075). The snRNA-seq libraries were sequenced on a Novaseq S2 with paired end reads (read 1: 26 bp, read 2: 96 bp) targeting 50,000 paired reads per nucleus.

snRNaseq Data Processing and Analysis—Raw single-nuclei RNA-seq data was processed using the 10X Genomics Cell Ranger (v3.0) pipeline. Reads were aligned to the Ensembl release 93 *Homo sapiens* genome. Cells were selected for downstream analysis using the cell barcodes associated with the most UMIs. We estimated the number of cells expected to be captured based on input nuclei concentration and retained this many cell barcodes for downstream analysis. Cells with < 200 unique genes detected were removed (gene detection: > 1 count). Cells with > 8% of their counts mapping to MT genes were removed. Genes detected in < 3 cells were removed. Normalization was performed using Seurat (v3.1 (Butler et al., 2018). Briefly, raw counts are read depth normalized by dividing by the total number of UMIs per cell, then multiplying by 10,000, adding a value of 1, and

Author Manuscript Author Manuscript Author Manuscript Author Manuscript

log transforming (ln (transcripts-per-10,000 + 1)). Raw UMI counts data were assessed for the effects from biological covariates (clinical dx, anatomical region, donor, age, sex), and technical covariates (RIN, PMI, library batch, number of UMI, number of genes detected, percentage MT). The effects of number of UMI (sequencing depth) were removed from the read depth normalized expression values using a linear model. One outlier sample was identified based on abnormal frequencies of major cell types and divergent gene expression patterns, and was removed from the analysis (Table S2). To isolate microglia cells for further analysis, clustering was performed using Seurat (v3.1) (Butler et al., 2018). Each cluster was then annotated as a major cell type using mean expression of groups of cell type marker genes, including the microglial markers CD74, CSF1R, C3 (Mathys et al., 2019), PTPRC, and DOCK8 (Kelley et al., 2018) (Figure S5A). Microglia clusters were selected for further analysis.

To identify genes affected by diagnosis, differentially expressed genes were determined using a linear model implemented in R comparing all disease microglia versus all control microglia (expression ~clinical_dx + number_umi). P values were then Benjamini-Hochberg corrected. We used the top 250 genes associated with bvFTD (at significance thresholds of beta > 0.1 and p-adjusted < 5.0 E-04) for further analysis (Table S3). We report the effect size output from the linear models as beta; which is approximate to the log2-fold change between groups (Table S3).

While RIN, PMI and age were not significantly different between case and control subjects (Mann Whitney U test; Table S2); sex and brank bank were not evenly split across groups (UCSF brain bank –bvFTD = 70%, control = 12%; male sex –bvFTD = 62%, controls = 50% (Table S2). To identify genes potentially affected by sex or brain bank in our analysis, differentially expressed genes were determined using a linear model comparing control microglia from males and females (expression ~sex + number_umi), and control microglia from UCSF versus University of Pennsylvania brain banks (expression ~finalsite + number_umi). We identified all genes significantly associated with either UCSF brain bank or sex using the thresholds applied to diagnosis (beta ^{3} 0.1, p value < 1.0 E-05, p-adjusted < 5.0 E-04) (Table S3) and excluded them from further analysis. To further identify genes potentially impacted by low tissue quality in our analysis, we ran independent linear models for post-mortem interval (PMI; expression ~pmi), RNA integrity (RIN; expression ~rin), number of genes detected per cell (expression ñumber_genes_detected), and number of UMI detected per cell (expression ~umi) using both case and control samples. No genes were significantly associated with PMI or number of genes or UMI detected; and genes found to be significantly associated with RIN (Table S3) were excluded from further analysis (beta >0.1, p value < 1.0 E-05, p-adjusted < 5.0 E-04).

In addition, to check that our findings were representative of group effects rather than driven by a few individuals, we compared all disease and control samples for average gene expression and total number of microglia contributed to the analysis (Figure S5E). In addition, to account for the random effect of subject in our analysis, we calculated differential expressed genes using a mixed effects model with subject as a random effect, and confirmed a very high Pearson's correlation between the diagnosis effects (beta) calculated from the linear model and mixed effects models (Figure 6B; Pearson's correlation

Author Manuscript Author Manuscript Author Manuscript Author Manuscript

= 0.89, p < 2.2e-16). These results confirm that the disease trends we report are representative of group differences (control versus disease) rather than based on a few non-representative individuals.

QUANTIFICATION AND STATISTICAL ANALYSIS

For each result, the figure legend describes the type of plot, statistical analysis, and sample n and definition. For all boxplots, the center line is at the median and the upper and lower lines are at the 75th and 25th percentiles, respectively (Figures 4I, 5C, 5F, 5K, S3B, S3C, S4G–S4I, and S5C). Results of tissue culture experiments show each sample data point as a separate dot, the center line at the group mean, and error bars showing s.e.m. (Figures 5D, 5G, and 5I) The barplot in Figure S2G has the center line at the group mean and error bars as s.e.m. In Figure S5D, the center line of the boxplot is the sample mean, the upper and lower lines are the 75th and 25th percentiles, respectively, and each dot is the average gene expression among the microglia from one subject, with the size of the dot proportional to the number of microglia contributing to the final analysis from that subject.

For each computational analysis performed from published code or resources, we used the statistical tests specified by the code and associated publications, as described and referenced under the corresponding experimental section under Methods Details. For single nuclear sequencing studies, the statistical approaches and methods, including for outlier removal and covariate analysis, are described in detail under the “single-nuclei RNA-seq data processing and analysis” subheading of Methods Details. Prior to single nuclear and RNA sequencing, samples were randomized across sample prep and library synthesis batches, and then randomized again across sequencing lanes to minimize sequencing batch effects. For cell culture experiments that measured one readout and compared one condition (Figure 5), a normal distribution was assumed and a two-tailed Student’s t test was performed; with samples paired if they were run together in an experimental batch. P values were corrected for multiple testing using FDR throughout the study, with significance values reported in the figures and figure legends.

Supplementary Material

Refer to Web version on PubMed Central for supplementary material.

ACKNOWLEDGMENTS

The results published here are in part based on data obtained from the AMP-AD Knowledge Portal (AMP-AD Knowledge Portal: https://doi.org/10.7303/syn2580853). We thank Eli Lilly and Company scientists for generating the rTg4510 microglia RNA-seq data (Wang et al., 2018) and providing us access to them. For the FTD GWAS summary statistics used for MAGMA, we acknowledge the investigators of the original study (Ferrari et al., 2014a). We thank Dr. Timothy Hammond and Dr. Marta Olah for use of their microglial single-cell data and discussion and Dr. Chris Hartl for helpful complementary analysis and discussion. Funding for this work was provided by Takeda Pharmaceuticals (D.H.G.), Rainwater Charitable Foundation (D.H.G. and W.W.S.), Roche Pharmaceuticals (D.H.G.), BrightFocus (D.H.G. and J.E.R), NIH grants to J.E.R and T.S.C. (5R25 NS065723) and J.E.R (K08 NS105916), Fineberg Foundation (J.E.R.), and the John Douglas French Alzheimer’s Foundation (J.E.R.). The UCSF Neurodegenerative Disease Brain Bank is supported by NIH grants AG023501 and AG019724, the Rainwater Charitable Foundation, and the Bluefield Project to Cure FTD. The University of Pennsylvania Center for Neurodegenerative Disease Research is supported by NIH grants P30-AG010123 Alzheimer’s Disease Core Center, U19-AG062418 Center on Alpha-synuclein Strains in Alzheimer Disease & Related Dementias, P01-AG017586 Frontotemporal Dementias: Genotypes and Phenotypes, U19-NS110456U54 Center without Walls for Imaging Proteinopathies with PET (CW2IP2), and U54-RFA-NS-19-030 Connect-TBI.

Author Manuscript Author Manuscript Author Manuscript Author Manuscript

REFERENCES

Ahmad S, Mu X, Yang F, Greenwald E, Park JW, Jacob E, Zhang CZ, and Hur S (2018). Breaching Self-Tolerance to Alu Duplex RNA Underlies MDA5-Mediated Inflammation. Cell 172, 797–810.e13. [PubMed: 29395326]

Ahmed ME, Iyer S, Thangavel R, Kempuraj D, Selvakumar GP, Raikwar SP, Zaheer S, and Zaheer A (2017). Co-Localization of Glia Maturation Factor with NLRP3 Inflammasome and Autophagosome Markers in Human Alzheimer's Disease Brain. J. Alzheimers Dis 60, 1143–1160. [PubMed: 28984607]

Allen M, Carrasquillo MM, Funk C, Heavner BD, Zou F, Younkin CS, Burgess JD, Chai HS, Crook J, Eddy JA, et al. (2016). Human whole genome genotype and transcriptome data for Alzheimer's and other neurodegenerative diseases. Sci. Data 3, 160089. [PubMed: 27727239]

Basters A, Knobeloch KP, and Fritz G (2018). USP18 - a multifunctional component in the interferon response. Biosci. Rep 38, BSR20180250.

Benjamini Y, and Hochberg Y (1995). Controlling the false discovery rate: a practical and powerful approach to multiple testing. J. R. Stat. Soc. B 57, 289–300.

Bussian TJ, Aziz A, Meyer CF, Swenson BL, van Deursen JM, and Baker DJ (2018). Clearance of senescent glial cells prevents tau-dependent pathology and cognitive decline. Nature 562, 578–582. [PubMed: 30232451]

Butler A, Hoffman P, Smibert P, Papalexi E, and Satija R (2018). Integrating single-cell transcriptomic data across different conditions, technologies, and species. Nat. Biotechnol 36, 411–420. [PubMed: 29608179]

Chandran V, Coppola G, Nawabi H, Omura T, Versano R, Huebner EA, Zhang A, Costigan M, Yekkirala A, Barrett L, et al. (2016). A Systems-Level Analysis of the Peripheral Nerve Intrinsic Axonal Growth Program. Neuron 89, 956–970. [PubMed: 26898779]

Chen JA, Wang Q, Davis-Turak J, Li Y, Karydas AM, Hsu SC, Sears RL, Chatzopoulou D, Huang AY, Wojta KJ, et al. (2015). A multiancestral genome-wide exome array study of Alzheimer disease, frontotemporal dementia, and progressive supranuclear palsy. JAMA Neurol 72, 414–422. [PubMed: 25706306]

Chen-Plotkin AS, Geser F, Plotkin JB, Clark CM, Kwong LK, Yuan W, Grossman M, Van Deerlin VM, Trojanowski JQ, and Lee VM (2008). Variations in the progranulin gene affect global gene expression in frontotemporal lobar degeneration. Hum. Mol. Genet 17, 1349–1362. [PubMed: 18223198]

Cuellar TL, Herzner AM, Zhang X, Goyal Y, Watanabe C, Friedman BA, Janakiraman V, Durinck S, Stinson J, Arnott D, et al. (2017). Silencing of retrotransposons by SETDB1 inhibits the interferon response in acute myeloid leukemia. J. Cell Biol 216, 3535–3549. [PubMed: 28887438]

de Leeuw CA, Mooij JM, Heskes T, and Posthuma D (2015). MAGMA: generalized gene-set analysis of GWAS data. PLOS Comput. Biol 11, e1004219. [PubMed: 25885710]

De Strooper B, and Karran E (2016). The Cellular Phase of Alzheimer's Disease. Cell 164, 603–615. [PubMed: 26871627]

Deczkowska A, Matcovitch-Natan O, Tsitsou-Kampeli A, Ben-Hamo S, Dvir-Szternfeld R, Spinrad A, Singer O, David E, Winter DR, Smith LK, et al. (2017). Mef2C restrains microglial inflammatory response and is lost in brain ageing in an IFN-I-dependent manner. Nat. Commun 8, 717. [PubMed: 28959042]

Deczkowska A, Keren-Shaul H, Weiner A, Colonna M, Schwartz M, and Amit I (2018). Disease-Associated Microglia: A Universal Immune Sensor of Neurodegeneration. Cell 173, 1073–1081. [PubMed: 29775591]

Dhir A, Dhir S, Borowski LS, Jimenez L, Teitell M, Rötig A, Crow YJ, Rice GI, Duffy D, Tamby C, et al. (2018). Mitochondrial double-stranded RNA triggers antiviral signalling in humans. Nature 560, 238–242. [PubMed: 30046113]

Dias Junior AG, Sampaio NG, and Rehwinkel J (2019). A Balancing Act: MDA5 in Antiviral Immunity and Autoinflammation. Trends Microbiol 27, 75–85. [PubMed: 30201512]

Author Manuscript Author Manuscript Author Manuscript Author Manuscript

Dobin A, Davis CA, Schlesinger F, Drenkow J, Zaleski C, Jha S, Batut P, Chaisson M, and Gingeras TR (2013). STAR: ultrafast universal RNA-seq aligner. Bioinformatics 29, 15–21. [PubMed: 23104886]

Doody GM, Care MA, Burgoyne NJ, Bradford JR, Bota M, Bonifer C, Westhead DR, and Tooze RM (2010). An extended set of PRDM1/BLIMP1 target genes links binding motif type to dynamic repression. Nucleic Acids Res 38, 5336–5350. [PubMed: 20421211]

Edwards FA (2019). A Unifying Hypothesis for Alzheimer's Disease: From Plaques to Neurodegeneration. Trends Neurosci 42, 310–322. [PubMed: 31006494]

Efthymiou AG, and Goate AM (2017). Late onset Alzheimer's disease genetics implicates microglial pathways in disease risk. Mol. Neurodegener 12, 43. [PubMed: 28549481]

Ferrari R, Hernandez DG, Nalls MA, Rohrer JD, Ramasamy A, Kwok JB, Dobson-Stone C, Brooks WS, Schofield PR, Halliday GM, et al. (2014a). Frontotemporal dementia and its subtypes: a genome-wide association study. Lancet Neurol 13, 686–699. [PubMed: 24943344]

Ferrari R, Ryten M, Simone R, Trabzuni D, Nicolaou N, Hondhamuni G, Ramasamy A, Vandrovcova J, UK Brain Expression Consortium; and Weale MEet al. (2014b). Assessment of common variability and expression quantitative trait loci for genome-wide associations for progressive supranuclear palsy. Neurobiol. Aging 35, 1514.e1–1514.e12. [PubMed: 24503276]

Frith MC, Fu Y, Yu L, Chen JF, Hansen U, and Weng Z (2004). Detection of functional DNA motifs via statistical over-representation. Nucleic Acids Res 32, 1372–1381. [PubMed: 14988425]

Gamache J, Benzow K, Forster C, Kemper L, Hlynialuk C, Furrow E, Ashe KH, and Koob MD (2019). Factors other than hTau overexpression that contribute to tauopathy-like phenotype in rTg4510 mice. Nat. Commun 10, 2479. [PubMed: 31171783]

Goldmann T, Zeller N, Raasch J, Kierdorf K, Frenzel K, Ketscher L, Basters A, Staszewski O, Brendecke SM, Spiess A, et al. (2015). USP18 lack in microglia causes destructive interferonopathy of the mouse brain. EMBO J 34, 1612–1629. [PubMed: 25896511]

Grubman A, Chew G, Ouyang JF, Sun G, Choo XY, McLean C, Simmons RK, Buckberry S, Vargas-Landin DB, Poppe D, et al. (2019). A single-cell atlas of entorhinal cortex from individuals with Alzheimer's disease reveals cell-type-specific gene expression regulation. Nat. Neurosci 22, 2087–2097. [PubMed: 31768052]

Guo C, Jeong HH, Hsieh YC, Klein HU, Bennett DA, De Jager PL, Liu Z, and Shulman JM (2018). Tau Activates Transposable Elements in Alzheimer's Disease. Cell Rep 23, 2874–2880. [PubMed: 29874575]

Haenseler W, Sansom SN, Buchrieser J, Newey SE, Moore CS, Nicholls FJ, Chintawar S, Schnell C, Antel JP, Allen ND, et al. (2017). A Highly Efficient Human Pluripotent Stem Cell Microglia Model Displays a Neuronal-Co-culture-Specific Expression Profile and Inflammatory Response. Stem Cell Reports 8, 1727–1742. [PubMed: 28591653]

Hammond TR, Dufort C, Dissing-Olesen L, Giera S, Young A, Wysoker A, Walker AJ, Gergits F, Segel M, Nemesh J, et al. (2019). Single-Cell RNA Sequencing of Microglia throughout the Mouse Lifespan and in the Injured Brain Reveals Complex Cell-State Changes. Immunity 50, 253–271.e6. [PubMed: 30471926]

Hansen KD, Irizarry RA, and Wu Z (2012). Removing technical variability in RNA-seq data using conditional quantile normalization. Biostatistics 13, 204–216. [PubMed: 22285995]

Heneka MT, Kummer MP, Stutz A, Delekate A, Schwartz S, Vieira-Saecker A, Griep A, Axt D, Remus A, Tzeng TC, et al. (2013). NLRP3 is activated in Alzheimer's disease and contributes to pathology in APP/PS1 mice. Nature 493, 674–678. [PubMed: 23254930]

Hickman SE, Kingery ND, Ohsumi TK, Borowsky ML, Wang LC, Means TK, and El Khoury J (2013). The microglial sensome revealed by direct RNA sequencing. Nat. Neurosci 16, 1896–1905. [PubMed: 24162652]

Höglinger GU, Melhem NM, Dickson DW, Sleiman PM, Wang LS, Klei L, Rademakers R, de Silva R, Litvan I, Riley DE, et al.; PSP Genetics Study Group (2011). Identification of common variants influencing risk of the tauopathy progressive supranuclear palsy. Nat. Genet 43, 699–705. [PubMed: 21685912]

Höing S, Rudhard Y, Reinhardt P, Glatza M, Stehling M, Wu G, Peiker C, Böcker A, Parga JA, Bunk E, et al. (2012). Discovery of inhibitors of microglial neurotoxicity acting through multiple

Author Manuscript Author Manuscript Author Manuscript Author Manuscript

mechanisms using a stem-cell-based phenotypic assay. Cell Stem Cell 11, 620–632. [PubMed: 23064101]

Honke N, Shaabani N, Zhang DE, Hardt C, and Lang KS (2016). Multiple functions of USP18. Cell Death Dis 7, e2444. [PubMed: 27809302]

Horn H, Lawrence MS, Chouinard CR, Shrestha Y, Hu JX, Worstell E, Shea E, Ilic N, Kim E, Kamburov A, et al. (2018). NetSig: network-based discovery from cancer genomes. Nat. Methods 15, 61–66. [PubMed: 29200198]

Ising C, Venegas C, Zhang S, Scheiblich H, Schmidt SV, Vieira-Saecker A, Schwartz S, Albasset S, McManus RM, Tejera D, et al. (2019). NLRP3 inflammasome activation drives tau pathology. Nature 575, 669–673. [PubMed: 31748742]

Jiang LQ, Xia T, Hu YH, Sun MS, Yan S, Lei CQ, Shu HB, Guo JH, and Liu Y (2018). IFITM3 inhibits virus-triggered induction of type I interferon by mediating autophagosome-dependent degradation of IRF3. Cell. Mol. Immunol 15, 858–867. [PubMed: 28435159]

Johansson JU, Woodling NS, Wang Q, Panchal M, Liang X, Trueba-Saiz A, Brown HD, Mhatre SD, Loui T, and Andreasson KI (2015). Prostaglandin signaling suppresses beneficial microglial function in Alzheimer's disease models. J. Clin. Invest. 125, 350–364. [PubMed: 25485684]

Johnson WE, Li C, and Rabinovic A (2007). Adjusting batch effects in microarray expression data using empirical Bayes methods. Biostatistics 8, 118–127. [PubMed: 16632515]

Kelley KW, Nakao-Inoue H, Molofsky AV, and Oldham MC (2018). Variation among intact tissue samples reveals the core transcriptional features of human CNS cell classes. Nat. Neurosci 21, 1171–1184. [PubMed: 30154505]

Keren-Shaul H, Spinrad A, Weiner A, Matcovitch-Natan O, Dvir-Szternfeld R, Ulland TK, David E, Baruch K, Lara-Astaiso D, Toth B, et al. (2017). A Unique Microglia Type Associated with Restricting Development of Alzheimer's Disease. Cell 169, 1276–1290.e17. [PubMed: 28602351]

Kigerl KA, de Rivero Vaccari JP, Dietrich WD, Popovich PG, and Keane RW (2014). Pattern recognition receptors and central nervous system repair. Exp. Neurol 258, 5–16. [PubMed: 25017883]

Kodama L, Guzman E, Etchegaray JI, Li Y, Sayed FA, Zhou L, Zhou Y, Zhan L, Le D, Udeochu JC, et al. (2020). Microglial microRNAs mediate sex-specific responses to tau pathology. Nat. Neurosci 23, 167–171. [PubMed: 31873194]

Lamb J, Crawford ED, Peck D, Modell JW, Blat IC, Wrobel MJ, Lerner J, Brunet JP, Subramanian A, Ross KN, et al. (2006). The Connectivity Map: using gene-expression signatures to connect small molecules, genes, and disease. Science 313, 1929–1935. [PubMed: 17008526]

Lambert JC, Ibrahim-Verbaas CA, Harold D, Naj AC, Sims R, Bellenguez C, DeStafano AL, Bis JC, Beecham GW, Grenier-Boley B, et al.; European Alzheimer's Disease Initiative (EADI); Genetic and Environmental Risk in Alzheimer's Disease; Alzheimer's Disease Genetic Consortium; Cohorts for Heart and Aging Research in Genomic Epidemiology (2013). Meta-analysis of 74,046 individuals identifies 11 new susceptibility loci for Alzheimer's disease. Nat. Genet 45, 1452–1458. [PubMed: 24162737]

Langfelder P, and Horvath S (2008). WGCNA: an R package for weighted correlation network analysis. BMC Bioinformatics 9, 559. [PubMed: 19114008]

Langfelder P, Luo R, Oldham MC, and Horvath S (2011). Is my network module preserved and reproducible? PLOS Comput. Biol 7, e1001057. [PubMed: 21283776]

Lee CYD, Daggett A, Gu X, Jiang LL, Langfelder P, Li X, Wang N, Zhao Y, Park CS, Cooper Y, et al. (2018). Elevated TREM2 Gene Dosage Reprograms Microglia Responsivity and Ameliorates Pathological Phenotypes in Alzheimer's Disease Models. Neuron 97, 1032–1048.e5. [PubMed: 29518357]

Li A, and Horvath S (2007). Network neighborhood analysis with the multinode topological overlap measure. Bioinformatics 23, 222–231. [PubMed: 17110366]

Liao Y, Smyth GK, and Shi W (2019). The R package Rsubread is easier, faster, cheaper and better for alignment and quantification of RNA sequencing reads. Nucleic Acids Res 47, e47. [PubMed: 30783653]

Litvinchuk A, Wan YW, Swartzlander DB, Chen F, Cole A, Propson NE, Wang Q, Zhang B, Liu Z, and Zheng H (2018). Complement C3aR Inactivation Attenuates Tau Pathology and Reverses an

Author Manuscript Author Manuscript Author Manuscript Author Manuscript

Immune Network Deregulated in Tauopathy Models and Alzheimer's Disease. Neuron 100, 1337–1353.e5. [PubMed: 30415998]

Lučiūnaitė A, McManus RM, Jankunec M, Rácz I, Dansokho C, Dalgėdienė I, Schwartz S, Brosseron F, and Heneka MT (2019). Soluble Aβ oligomers and protofibrils induce NLRP3 inflammasome activation in microglia. J. Neurochem (12 23), e14945. [PubMed: 31872431]

Mao R, Yang R, Chen X, Harhaj EW, Wang X, and Fan Y (2017). Regnase-1, a rapid response ribonuclease regulating inflammation and stress responses. Cell. Mol. Immunol 14, 412–422. [PubMed: 28194024]

Marazzi I, Ho JS, Kim J, Manicassamy B, Dewell S, Albrecht RA, Seibert CW, Schaefer U, Jeffrey KL, Prinjha RK, et al. (2012). Suppression of the antiviral response by an influenza histone mimic. Nature 483, 428–433. [PubMed: 22419161]

Mathys H, Adaikkan C, Gao F, Young JZ, Manet E, Hemberg M, De Jager PL, Ransohoff RM, Regev A, and Tsai LH (2017). Temporal Tracking of Microglia Activation in Neurodegeneration at Single-Cell Resolution. Cell Rep 21, 366–380. [PubMed: 29020624]

Mathys H, Davila-Velderrain J, Peng Z, Gao F, Mohammadi S, Young JZ, Menon M, He L, Abdurrob F, Jiang X, et al. (2019). Single-cell transcriptomic analysis of Alzheimer's disease. Nature 570, 332–337. [PubMed: 31042697]

Matys V, Fricke E, Geffers R, Gössling E, Haubrock M, Hehl R, Hornischer K, Karas D, Kel AE, Kel-Margoulis OV, et al. (2003). TRANSFAC: transcriptional regulation, from patterns to profiles. Nucleic Acids Res 31, 374–378. [PubMed: 12520026]

Moore Z, Mobilio F, Walker FR, Taylor JM, and Crack PJ (2020). Abrogation of type-I interferon signalling alters the microglial response to $A\beta_{1-42}$. Sci. Rep 10, 3153. [PubMed: 32081950]

Mudò G, Frinchi M, Nuzzo D, Scaduto P, Plescia F, Massenti MF, Di Carlo M, Cannizzaro C, Cassata G, Cicero L, et al. (2019). Anti-inflammatory and cognitive effects of interferon-b1a (IFNb1a) in a rat model of Alzheimer's disease. J. Neuroinflammation 16, 44. [PubMed: 30777084]

Olah M, Menon V, Habib N, Taga M, Yung C, Cimpean M, Khairalla A, Dionne D, Hopp S, Frosch M, et al. (2018). A single cell-based atlas of human microglial states reveals associations with neurological disorders and histopathological features of the aging brain. bioRxiv 10.1101/343780.

Onishi T, Matsumoto Y, Hattori M, Obayashi Y, Nakamura K, Yano T, Horiguchi T, and Iwashita H (2014). Early-onset cognitive deficits and axonal transport dysfunction in P301S mutant tau transgenic mice. Neurosci. Res 80, 76–85. [PubMed: 24406748]

Pampuscenko K, Morkuniene R, Sneideris T, Smirnovas V, Budvytyte R, Valincius G, Brown GC, and Borutaite V (2020). Extracellular tau induces microglial phagocytosis of living neurons in cell cultures. J. Neurochem 154, 316–329. [PubMed: 31834946]

Portales-Casamar E, Thongjuea S, Kwon AT, Arenillas D, Zhao X, Valen E, Yusuf D, Lenhard B, Wasserman WW, and Sandelin A (2010). JASPAR 2010: the greatly expanded open-access database of transcription factor binding profiles. Nucleic Acids Res 38, D105–D110. [PubMed: 19906716]

Renkl AC, Wussler J, Ahrens T, Thoma K, Kon S, Uede T, Martin SF, Simon JC, and Weiss JM (2005). Osteopontin functionally activates dendritic cells and induces their differentiation toward a Th1-polarizing phenotype. Blood 106, 946–955. [PubMed: 15855273]

Rivals I, Personnaz L, Taing L, and Potier MC (2007). Enrichment or depletion of a GO category within a class of genes: which test? Bioinformatics 23, 401–407. [PubMed: 17182697]

Rock RB, Hu S, Deshpande A, Munir S, May BJ, Baker CA, Peterson PK, and Kapur V (2005). Transcriptional response of human microglial cells to interferon-gamma. Genes Immun 6, 712–719. [PubMed: 16163375]

Rossin EJ, Lage K, Raychaudhuri S, Xavier RJ, Tatar D, Benita Y, Cotsapas C, and Daly MJ; International Inflammatory Bowel Disease Genetics Consortium (2011). Proteins encoded in genomic regions associated with immune-mediated disease physically interact and suggest underlying biology. PLOS Genet 7, e1001273. [PubMed: 21249183]

Roy ER, Wang B, Wan YW, Chiu G, Cole A, Yin Z, Propson NE, Xu Y, Jankowsky JL, Liu Z, et al. (2020). Type I interferon response drives neuroinflammation and synapse loss in Alzheimer disease. J. Clin. Invest 130, 1912–1930. [PubMed: 31917687]

Author Manuscript Author Manuscript Author Manuscript Author Manuscript

Saito R, Smoot ME, Ono K, Ruscheinski J, Wang PL, Lotia S, Pico AR, Bader GD, and Ideker T (2012). A travel guide to Cytoscape plugins. Nat. Methods 9, 1069–1076. [PubMed: 23132118]

Santacruz K, Lewis J, Spires T, Paulson J, Kotilinek L, Ingelsson M, Guimaraes A, DeTure M, Ramsden M, McGowan E, et al. (2005). Tau suppression in a neurodegenerative mouse model improves memory function. Science 309, 476–481. [PubMed: 16020737]

Saura J, Tusell JM, and Serratosa J (2003). High-yield isolation of murine microglia by mild trypsinization. Glia 44, 183–189. [PubMed: 14603460]

Schafer DP, Lehrman EK, and Stevens B (2013). The "quad-partite" synapse: microglia-synapse interactions in the developing and mature CNS. Glia 61, 24–36. [PubMed: 22829357]

Scott CL, T'Jonck W, Martens L, Todorov H, Sichien D, Soen B, Bonnardel J, De Prijck S, Vandamme N, Cannoodt R, et al. (2018). The Transcription Factor ZEB2 Is Required to Maintain the Tissue-Specific Identities of Macrophages. Immunity 49, 312–325.e5. [PubMed: 30076102]

Shi Y, Manis M, Long J, Wang K, Sullivan PM, Remolina Serrano J, Hoyle R, and Holtzman DM (2019). Microglia drive APOE-dependent neurodegeneration in a tauopathy mouse model. J. Exp. Med 216, 2546–2561. [PubMed: 31601677]

Sloan SA, Andersen J, Paşca AM, Birey F, and Paşca SP (2018). Generation and assembly of human brain region-specific three-dimensional cultures. Nat. Protoc 13, 2062–2085. [PubMed: 30202107]

Snell LM, McGaha TL, and Brooks DG (2017). Type I Interferon in Chronic Virus Infection and Cancer. Trends Immunol 38, 542–557. [PubMed: 28579323]

Song WM, and Colonna M (2018). The identity and function of microglia in neurodegeneration. Nat. Immunol 19, 1048–1058. [PubMed: 30250185]

Srinivasan K, Friedman BA, Larson JL, Lauffer BE, Goldstein LD, Appling LL, Borneo J, Poon C, Ho T, Cai F, et al. (2016). Untangling the brain's neuroinflammatory and neurodegenerative transcriptional responses. Nat. Commun 7, 11295. [PubMed: 27097852]

Stancu IC, Cremers N, Vanrusselt H, Couturier J, Vanoosthuyse A, Kessels S, Lodder C, Brône B, Huaux F, Octave JN, et al. (2019). Aggregated Tau activates NLRP3-ASC inflammasome exacerbating exogenously seeded and non-exogenously seeded Tau pathology in vivo. Acta Neuropathol 137, 599–617. [PubMed: 30721409]

Stark C, Breitkreutz BJ, Reguly T, Boucher L, Breitkreutz A, and Tyers M (2006). BioGRID: a general repository for interaction datasets. Nucleic Acids Res 34, D535–D539. [PubMed: 16381927]

Subramanian A, Narayan R, Corsello SM, Peck DD, Natoli TE, Lu X, Gould J, Davis JF, Tubelli AA, Asiedu JK, et al. (2017). A Next Generation Connectivity Map: L1000 Platform and the First 1,000,000 Profiles. Cell 171, 1437–1452.e17. [PubMed: 29195078]

Sun W, Samimi H, Gamez M, Zare H, and Frost B (2018). Pathogenic tau-induced piRNA depletion promotes neuronal death through transposable element dysregulation in neurodegenerative tauopathies. Nat. Neurosci 21, 1038–1048. [PubMed: 30038280]

Swarup V, Hinz FI, Rexach JE, Noguchi KI, Toyoshiba H, Oda A, Hirai K, Sarkar A, Seyfried NT, Cheng C, et al.; International Frontotemporal Dementia Genomics Consortium (2019). Identification of evolutionarily conserved gene networks mediating neurodegenerative dementia. Nat. Med 25, 152–164. [PubMed: 30510257]

Szklarczyk D, Morris JH, Cook H, Kuhn M, Wyder S, Simonovic M, Santos A, Doncheva NT, Roth A, Bork P, et al. (2017). The STRING database in 2017: quality-controlled protein-protein association networks, made broadly accessible. Nucleic Acids Res 45 (D1), D362–D368. [PubMed: 27924014]

Taylor JP, Cash MN, Santostefano KE, Nakanishi M, Terada N, and Wallet MA (2018). CRISPR/Cas9 knockout of USP18 enhances type I IFN responsiveness and restricts HIV-1 infection in macrophages. J. Leukoc. Biol 103, 1225–1240.

Teijaro JR, Ng C, Lee AM, Sullivan BM, Sheehan KC, Welch M, Schreiber RD, de la Torre JC, and Oldstone MB (2013). Persistent LCMV infection is controlled by blockade of type I interferon signaling. Science 340, 207–211. [PubMed: 23580529]

Vénéreau E, Ceriotti C, and Bianchi ME (2015). DAMPs from Cell Death to New Life. Front. Immunol 6, 422. [PubMed: 26347745]

Author Manuscript Author Manuscript Author Manuscript Author Manuscript

Wang Y, Cella M, Mallinson K, Ulrich JD, Young KL, Robinette ML, Gilfillan S, Krishnan GM, Sudhakar S, Zinselmeyer BH, et al. (2015). TREM2 lipid sensing sustains the microglial response in an Alzheimer's disease model. Cell 160, 1061–1071. [PubMed: 25728668]

Wang H, Li Y, Ryder JW, Hole JT, Ebert PJ, Airey DC, Qian HR, Logsdon B, Fisher A, Ahmed Z, et al. (2018). Genome-wide RNAseq study of the molecular mechanisms underlying microglia activation in response to pathological tau perturbation in the rTg4510 tau transgenic animal model. Mol. Neurodegener 13, 65. [PubMed: 30558641]

Wölfl M, Schwinn S, Yoo YE, Reß ML, Braun M, Chopra M, Schreiber SC, Ayala VI, Ohlen C, Eyrich M, et al. (2013). Src-kinase inhibitors sensitize human cells of myeloid origin to Toll-like-receptor-induced interleukin 12 synthesis. Blood 122, 1203–1213. [PubMed: 23836556]

Woodling NS, Wang Q, Priyam PG, Larkin P, Shi J, Johansson JU, Zagol-Ikapitte I, Boutaud O, and Andreasson KI (2014). Suppression of Alzheimer-associated inflammation by microglial prostaglandin-E2 EP4 receptor signaling. J. Neurosci 34, 5882–5894. [PubMed: 24760848]

Wykes MN, and Lewin SR (2018). Immune checkpoint blockade in infectious diseases. Nat. Rev. Immunol 18, 91–104. [PubMed: 28990586]

Zambon AC, Gaj S, Ho I, Hanspers K, Vranizan K, Evelo CT, Conklin BR, Pico AR, and Salomonis N (2012). GO-Elite: a flexible solution for pathway and ontology over-representation. Bioinformatics 28, 2209–2210. [PubMed: 22743224]

Zhang Y, Chen K, Sloan SA, Bennett ML, Scholze AR, O'Keeffe S, Phatnani HP, Guarnieri P, Caneda C, Ruderisch N, et al. (2014). An RNA-sequencing transcriptome and splicing database of glia, neurons, and vascular cells of the cerebral cortex. J. Neurosci 34, 11929–11947. [PubMed: 25186741]

Author Manuscript Author Manuscript Author Manuscript Author Manuscript

Highlights

- Significant changes in microglial-immune signaling mark stages of neurodegeneration
- Pro-inflammatory pathways yield to early interferon-driven immune suppression
- A key hub in the immune suppression module, USP18, modulates this response
- Validation of chemogenetic predictions identifies drugs modulating microglial function

Author Manuscript Author Manuscript Author Manuscript Author Manuscript

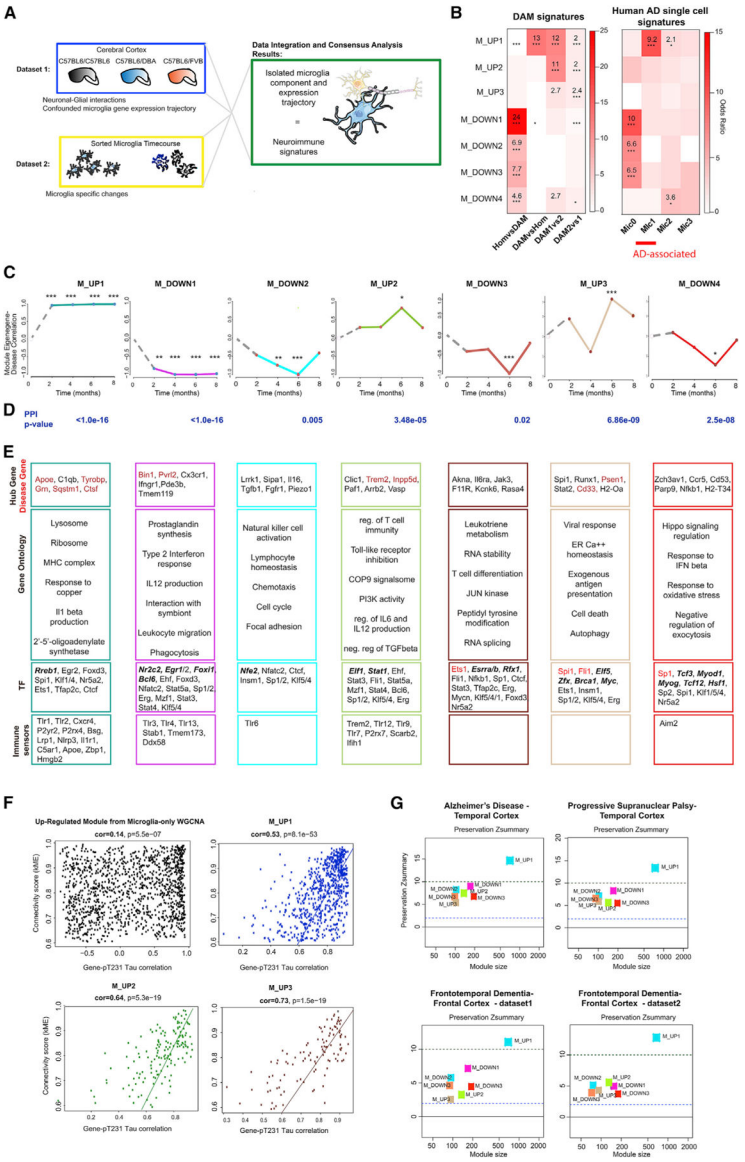

Figure 1. Purified Microglia-Brain Tissue Consensus Gene Co-expression Network Analysis

(A) Experimental schema, showing approach for microglia-tissue consensus WGCNA.

(B) Module enrichment heatmap for (left) top 100 genes differentially expressed between progressive microglia single-cell states, as indicated, and (right) genes differentially expressed between microglia single-cell states identified from the prefrontal cortex of patients with Alzheimer's disease (AD) and controls, as indicated; Mic0, Mic1 (AD-associated microglia subpopulation), Mic2, and Mic3, microglia subclusters as defined in Mathys et al. (2019); n = 7 modules with 4 comparisons per module. *FDR < 0.05, **FDR < 0.005, ***FDR < 0.001. Hom, homeostatic; DAM1, type 1 disease-associated microglia; DAM2, type 2 DAMs, as defined in Keren-Shaul et al. (2017).

(C) Signed Pearson's correlation of the module eigengene (ME) with transgenic condition calculated in the rTg4510 microglia gene expression dataset at each age; unpaired 2-tailed t

Author Manuscript Author Manuscript Author Manuscript Author Manuscript

test; n = 7 modules, n = 4 mice per genotype (P301L *MAPT* or wild type [WT]); *p < 0.05, **p < 0.01, ***p < 0.005. Graphed with theoretical zero plotted at time zero.

(D) Module PPI network enrichment p value (STAR Methods).

(E) Module annotation showing representative module hub genes (disease genes in red), enriched Gene Ontology terms (*Z* score > 2), transcription factors (TFs) with binding site enrichment (p < 0.05; STAR Methods), and module genes that function as receptors for pathogen- or damage-associated molecular patterns ("immune sensors"). TF labels are bold and italic if unique, and red if a module hub gene.

(F) Scatterplot of gene-module connectivity (kME) (y axis) versus gene correlation with sample pT231 tau levels (x axis) in TPR50 mouse brain (n = 36; frontal cortex, 6 months of age, n = 18 per group of WT or P301S *MAPT*; p values from 2-sided test for Pearson correlation).

(G) Module preservation in AD patient and control temporal cortex (control n = 74, AD n = 86), PSP patient and control temporal cortex (control n = 37, PSP n = 37) (Allen et al., 2016), and FTD patient and control frontal cortex (dataset 1 [Chen-Plotkin et al., 2008] control n = 8, FTD n = 10; dataset 2 [Swarup et al., 2019] control n = 14, FTD n = 16). The bottom line is at the lower cutoff for preservation (Zsummary = 2) and the upper line is at the cutoff for high preservation (Zsummary = 10) (Langfelder et al., 2011).

See also Figure S1.

Author Manuscript Author Manuscript Author Manuscript Author Manuscript

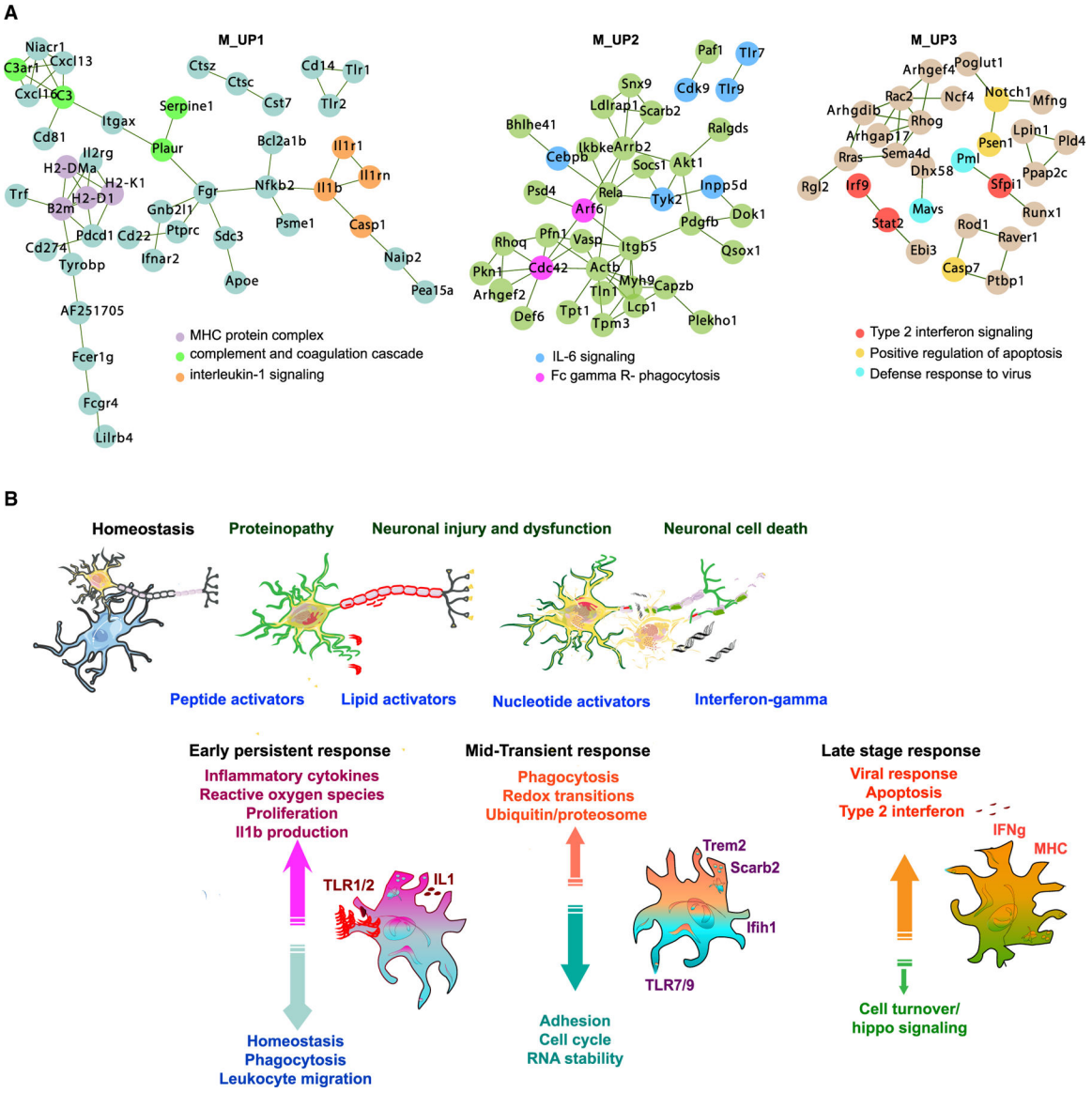

Figure 2. Microglia-Tissue Consensus Module Microglia Disease Time Course and Pathway Annotation

(A) Protein-protein interactions (PPIs) among the top 150 module genes (ranked by kME) with associated Gene Ontology pathway labeled, as shown (GO-Elite [Zambon et al., 2012], *Z* score > 2).

(B) Model showing microglia transitions across progressive disease stages based on the annotation of microglia-tissue consensus modules (MNMs).

See also Figure S2.

Author Manuscript Author Manuscript Author Manuscript Author Manuscript

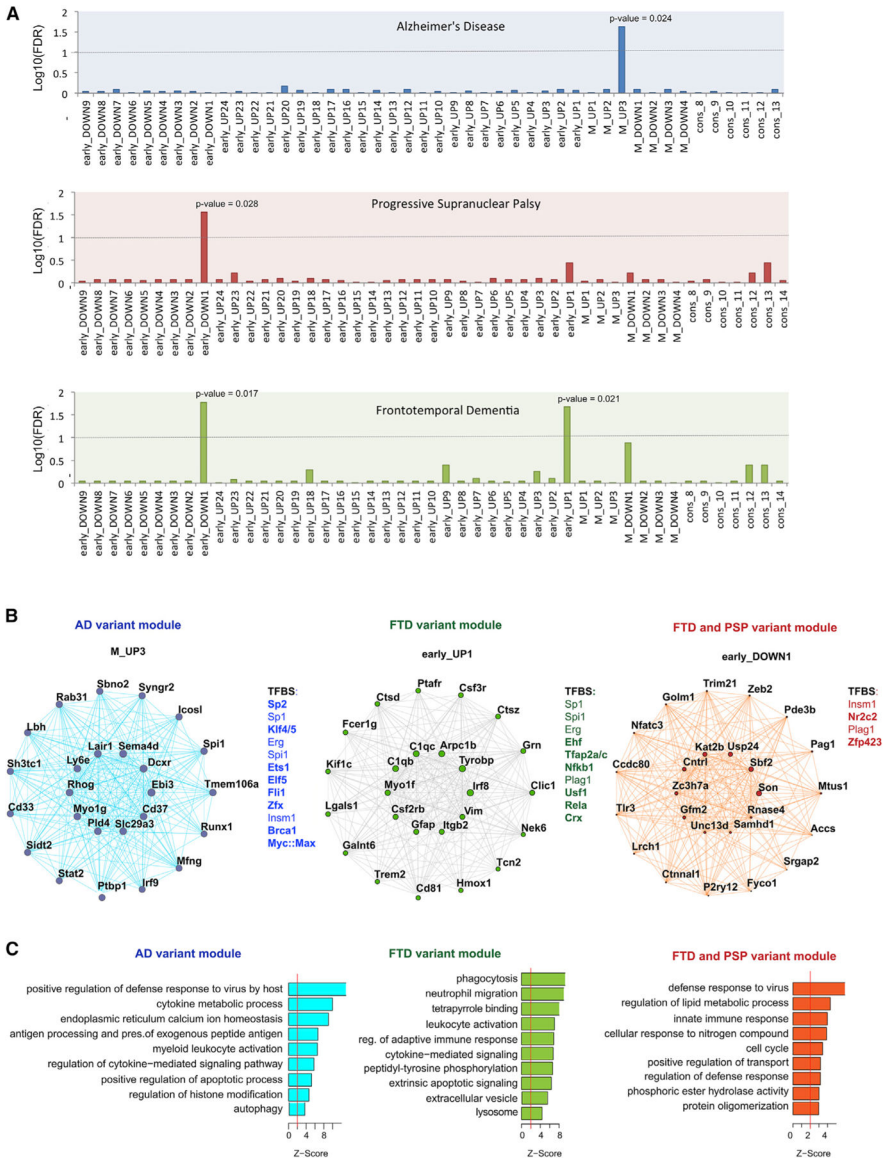

Figure 3. GWAS Variants for AD, FTD, or PSP Implicate Modules Associated with Viral Response in Causal Disease Biology

(A) Module enrichment for disease variants for AD (Lambert et al., 2013), FTD (Ferrari et al., 2014b), or PSP (Höglinger et al., 2011) (horizontal line: —log10(FDR) = 1; FDR corrected, competitive gene-set analysis p value from MAGMA [de Leeuw et al., 2015]).

(B) Gene co-expression network plots of the top 25 genes, ranked by kME, from each module; with enriched TFs (bold, if unique) shown ("TFBS"; enrichment $p < 0.05$).

(C) GO terms enrichment among corresponding module genes (Z score > 2).

See also Figure S3.

Author Manuscript Author Manuscript Author Manuscript Author Manuscript

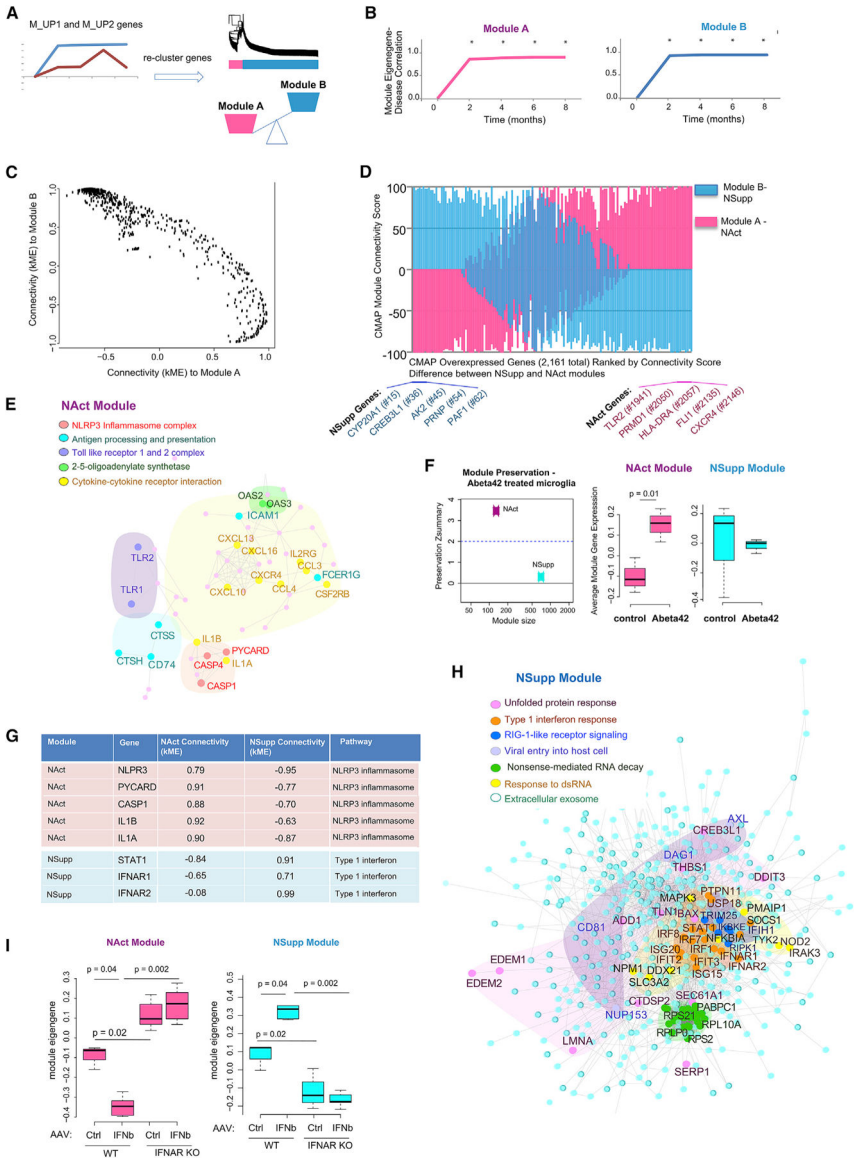

Figure 4. Opposing Neuroimmune Activation and Suppression Modules Are Upregulated Early in Disease

(A) Experimental schema for identifying opposing regulatory networks among upregulated microglia module genes.

(B) Signed Pearson's correlation of the ME with transgenic trait calculated in the rTg4510 microglia gene expression dataset at each age (n = 7 modules, n = 4 mice per genotype [P301L *MAPT* or WT], ages = 2, 4, 6, and 8 months, *2-tailed p value of Pearson's correlation < 0.005).

(C) Scatterplot of gene-module connectivity scores (kME) with module A and module B calculated across rTg4510 purified microglia samples (n = 32 samples, n = 899 genes).

(D) Bar plots showing CMAP connectivity scores between overexpression of a given gene (n = 2,161 genes) and NAct (pink) and NSupp (blue) modules, ordered from left to right by difference between NSupp and NAct module connectivity scores. The top 5 highest scoring module genes among 2,161 CMAP overexpressed genes shown for each module.

Author Manuscript Author Manuscript Author Manuscript Author Manuscript

(E) PPI maps with associated GO pathways highlighted for NAct.
(F) Module preservation and trajectory of average module gene expression of the NAct and NSupp modules in cultured microglia treated with fibrillar Abeta42 or vehicle control (unpaired 2-sample Wilcoxon rank-sum test; n = 3 per group [Woodling et al., 2014]). Boxplot with center line at median and upper and lower lines at 75th and 25th percentiles.
(G) Module assignment and module connectivity scores for components of NLRP3 inflammasome complex and type I IFN response.
(H) PPI maps with associated GO pathways highlighted for NSupp.
(I) Trajectory of NAct and NSupp MEs in mouse microglia purified from IFNAR knockout or WT mice infected with IFN-β expressing or control adeno-associated virus (AAV) (unpaired 2-sample Wilcoxon rank-sum test, WT control-virus n = 3, IFNAR knockout control-virus n = 7, WT IFN-β-virus n = 5, IFNAR knockout IFN-β-virus n = 7 [Deczkowska et al., 2017]). Boxplot with center line at median and upper and lower lines at 75th and 25th percentiles.
See also Figure S4.

Author Manuscript Author Manuscript Author Manuscript Author Manuscript

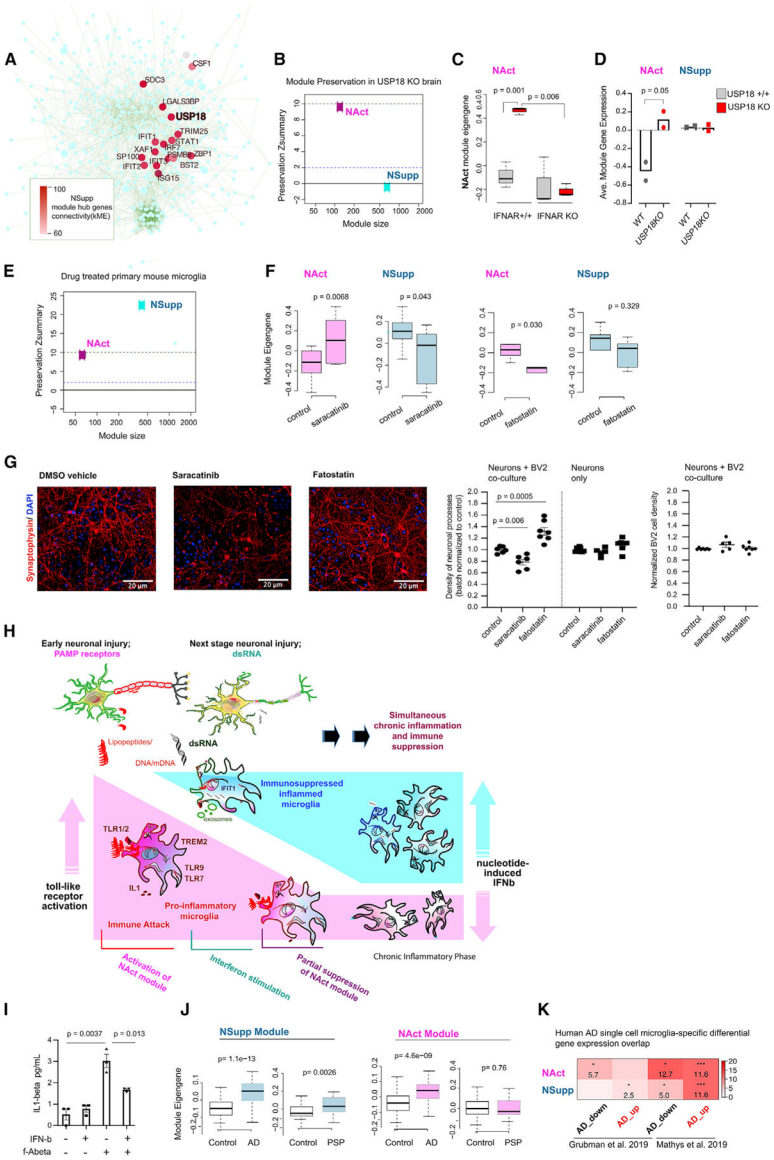

Figure 5. Microglial Immune Suppression Is Prominent in Disease

(A) PPI plot showing that *Usp18* is a central NSupp module gene based on high PPI and ME connectivity (node color) in microglia purified from IFN-β and control treated mice (Deczkowska et al., 2017).

(B–D) Module preservation of NAct and NSupp modules (B); ME trajectory of NAct in *Usp18* knockout, IFNAR knockout, double knockout, and WT mouse brain (C) (2-tailed unpaired t test; n = 3 per group [Goldmann et al., 2015]; boxplot with center line at median and upper and lower lines at 75th and 25th percentiles) and average module gene expression of NSupp and NAct in *Usp18* knockout and WT mouse microglia (D) (2-tailed unpaired t test; n = 2 per group [Goldmann et al., 2015]).

(E) Module preservation of NAct and NSupp in primary mouse microglia cultures treated with drugs or DMSO vehicle as indicated in (F).

Author Manuscript Author Manuscript Author Manuscript Author Manuscript

(F) ME trajectory of NAct and NSupp in primary mouse microglia cultures treated with high-dose saracatinib (1 μM, n = 10, 24 h) or DMSO vehicle control (n = 10, 24 h), and fatostatin (1 μM, n = 5, 72 h) or DMSO vehicle (n = 6, 72 h) (unpaired 2-sample Wilcoxon rank-sum test).

(G) Image of neuronal-BV2 co-cultures (left) showing neuronal processes (synaptophysin) and BV2 cells (non-neuronal $DAPI^+$ cells), and density of neuronal processes (left) and BV2 cells (far right) normalized to controls, following 36 h co-culture and treatment with saracatinib (1 μM, n = 5), fatostatin (1 μM n = 7), or DMSO vehicle (n = 6), compared to density of neuronal processes in drug-treated and control neurons cultured without BV2 cells (center).

(H) Model showing that nucleotide detection from damaged cells activates interferon (IFN) to suppress microglia activity in disease.

(I) Pre-treatment with IFN-β (20 ng/mL) reduces IL-1β secretion of human iPSC-derived microglia-like cultures following stimulation by fibrillar amyloid β (1 μM) (2-tailed unpaired t test; n = 3 per condition).

(J) ME trajectories of NSupp and NAct in AD patient and control temporal cortex (control n = 74, AD n = 86) and PSP patient and control temporal cortex (control n = 37, PSP n = 37) (Allen et al., 2016) (unpaired 2-sample Wilcoxon rank-sum test). Boxplot with center line at median and upper and lower lines at 75th and 25th percentiles.

(K) Module enrichment for genes that are differentially expressed in microglia of AD compared to control brain based on published single nuclear sequencing studies (genes upregulated or downregulated in AD with log fold change [LFC] > 0.1 and FDR < 0.05 = “AD_up,” and “AD_down,” respectively; Fisher’s 2-tailed exact test, *FDR < 0.05, **FDR < 0.001, ***FDR < 0.005 [Grubman et al., 2019; Mathys et al., 2019]).

Author Manuscript Author Manuscript Author Manuscript Author Manuscript

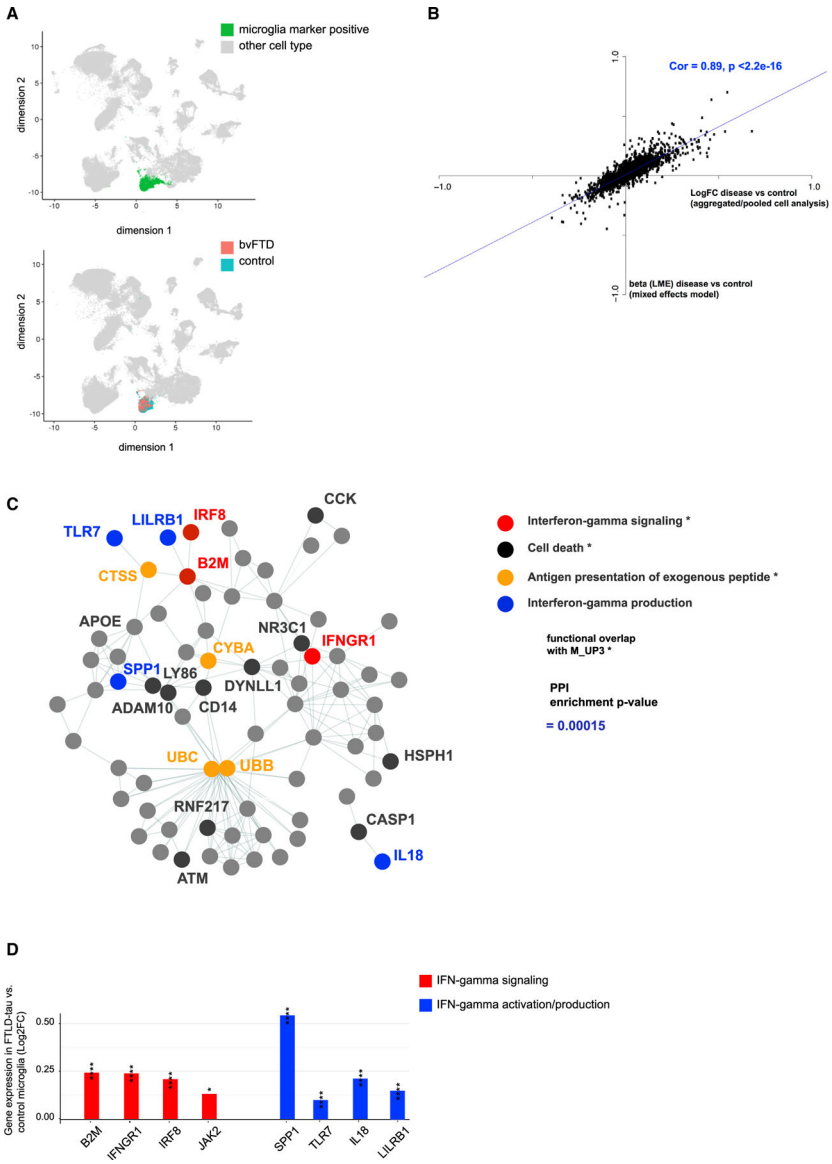

Figure 6. Microglia from Patients with FTD Upregulate the Later-Stage Immune Pathways Identified in Mice with Tau Pathology

(A) Seurat object of nuclei sequenced from bvFTD patients with tau pathology (Pick's disease, precentral gyrus, n = 7) and control (no pathology, precentral gyrus, n = 8), showing the cell cluster enriched for microglial-specific marker genes (green, top) and cells from bvFTD (pink) and control (blue) patients.

(B) Scatterplot and Pearson's correlation of effect size (β) of differential gene expression between bvFTD versus control microglia, comparing results from a linear model (x axis) and mixed-effects model with subject as a random effect (y axis) (n = 7,989 genes).

(C) PPI plot of genes significantly upregulated in bvFTD microglia compared to controls ($log2fc^3$ 0.1, FDR < 5E−4), highlighting genes with PPI in significant GO pathways ($Z > 2$). The asterisk indicates functional overlap with M_UP3.

Author Manuscript Author Manuscript Author Manuscript Author Manuscript

(D) Bar plot of genes that are differentially expressed in bvFTD versus control microglia (log2fc scale) and either activate IFN-γ (blue) or mediate IFN-γ signaling (red), (linear model; *p < 0.05, **p < 0.01, ***p < 0.001, ****p < 0.001).
See also Figure S5 and Table S3.

Author Manuscript Author Manuscript Author Manuscript Author Manuscript

KEY RESOURCES TABLE

REAGENT or RESOURCE	SOURCE	IDENTIFIER
Antibodies		
Rabbit anti-Iba1	WAKO	Cat# 019–19741; RRID:AB_839504
Guinea pig anti-synaptophysin	Synaptic Systems	Cat# 101 004; RRID:AB_1210382
Donkey anti-rabbit Alexa Fluor 488	Thermo Fisher	Cat# A-21206; RRID:AB_2535792
Goat anti-guinea pig Alexa Fluor 555	Thermo Fisher	Cat# A-21435; RRID:AB_2535856
Biological Samples		
Human Postmortem Precentral Gyrus Tissue Samples (Pick's disease, and control)	UCSF Neurodegenerative Disease Brain Bank; University of Pennsylvania Center for Neurodegenerative Disease Research Brain Bank	N/A
Chemicals, Peptides, and Recombinant Proteins		
DMEM-F12 Media	Thermo Fisher	Cat# 10569044
Heat-inactivated FBS	Thermo Fisher	Cat# 16140071
GlutaMAX Supplement	Life Technologies	Cat# 35050–061
B-27 Supplement (without Vitamin A)	Thermo Fisher	Cat# 17504–044
Neurobasal-A Media	Life Technologies	Cat# 10888–022
Essential 8 + supplement	Thermo Fisher	Cat# A15170001
RPMI Media	Thermo Fisher	Cat# 11875085
AIM-V Media	Thermo Fisher	Cat# 12055083
N2 Supplement	Thermo Fisher	Cat# 17502048
HBSS (without calcium, magnesium)	Thermo Fisher	Cat# 14175095
DNase I	Roche	Cat# 4536282001
Penicillin/Streptomycin	Thermo Fisher	Cat# 15140122
Beta-mercaptoethanol	Thermo Fisher	Cat# 31350–010
Poly-D-Lysine	Sigma	Cat# A-003-M
Recombinant Human IL-34 Protein	Biolegend	Cat# 577906
Recombinant Human GM-CSF	Biolegend	Cat# 766104
Recombinant Human IFN-beta	R&D Systems	Cat# 8499-IF
Recombinant Human IL-3	Biolegend	Cat# 578006
Recombinant Human M-CSF	Biolegend	Cat# 574806
Recombinant Human BMP-4 (*E. coli* derived)	Peprotech	Cat# 120–05ET
Recombinant Human VEGF-165	Biolegend	Cat# 583702
Recombinant Human SCF	Peprotech	Cat# 300–07
Recombinant Vitronectin (VTN-N)	Thermo Fisher	Cat# A14700
Rock Inhibitor (Y-27632 dihydrochloride)	Tocris	Cat# 1254
Saractinib	Selleckchem	Cat# S1006
Fatostatin hydrobromide	Sigma	Cat# F893
Dimethyl sulfoxide (DMSO)	Sigma	Cat# D2650

Author Manuscript Author Manuscript Author Manuscript Author Manuscript

REAGENT or RESOURCE	SOURCE	IDENTIFIER
Amyloid beta (abeta, 1–42)	Bachem	Cat# 4014447
Recombinant Human IFN-beta	R&D Systems	Cat# 8499-IF
Complete protease inhibitor cocktail	Roche	Cat# 11697498001
OptiPrep (Iodixanol)	StemCell Technologies	Cat# 07820
Triton X-100	Fisher	Cat# 21568–0010
Tween-20	Sigma	Cat# P9416
RNase-free Bovine Serum Albumin (BSA)	VWR	Cat# EM-2930
RNase Inhibitor	NEB	Cat# M0314
DNase I	Roche	Cat# 4536282001
Critical Commercial Assays		
NucleoSpin RNA Plus	Takara	Cat# 740984.50
QuantSeq 3′ End Labeling Kit	Lexogen	Cat# 015.96
Total Tau Human ELISA Kit	Thermo Fisher	Cat# KHB0041
pT231 Tau Human ELISA Kit	Thermo Fisher	Cat# KHB8051
IL-1beta Mouse ELISA Kit	R&D Systems	Cat# DY401
Chromium Single Cell 3′ Reagent Kits V2	10X Genomics	Cat# 1000075
Deposited Data		
TPR50 Mouse (male P301S MAPT and WT) microarray or RNaseq transcriptomics dataset	(Swarup et al., 2019)	GEO: GSE90696
rTg4510 microglia dataset	(Wang et al., 2018)	AMP-AD Knowledge Portal: https://www.synapse.org/#!Synapse:syn9884351
JNPL3 mouse datasets	AMP-AD	AMP-AD Knowledge Portal: https://adknowledgeportal.synapse.org/Explore/Studies/DetailsPage?Study=syn3157182
PS2APP microglia RNaseq	(Srinivasan et al., 2016)	GEO: GSE75431
USP18 Knockout and IFNAR Knockout	(Goldmann et al., 2015)	GEO: GSE61499; GEO: GSE61500
5xFAD microglia RNaseq	(Wang et al., 2015)	GEO: GSE65067
CK-p25	(Mathys et al., 2017)	GEO: GSE103334
In vivo Abeta-42	(Johansson et al., 2015)	GEO: GSE57181
in vitro treatments with Abeta-42	(Woodling et al., 2014)	GEO: GSE55627
Microglia isolated from IFN-beta AAV infected mouse brain	(Deczkowska et al., 2017)	GEO: GSE98401
IFN-gamma human microglia	(Rock et al., 2005)	GEO: GSE1432
Human postmortem data-FTD RNaseq	(Chen-Plotkin et al., 2008)	GEO: GSE13162
Human postmortem data-AD and PSP temporal cortex	(Allen et al., 2016)	AMP-AD Knowledge Portal: https://repo-prod.prod.sagebase.org/repo/v1/doi/locate?id=syn3163039&type=ENTITY
Human postmortem data-FTD frontal cortex	(Swarup et al., 2019)	Synpase: https://www.synapse.org/#!Synapse:syn7818788
Single nuclear sequencing data from Alzheimer's and control prefrontal cortex	(Mathys et al., 2019)	Synpase: https://www.synapse.org/#!Synapse:syn18485175
Single nuclear sequencing data from Alzheimer's and control Entorhinal cortex	(Grubman et al., 2019)	GEO: GSE138852
Single cell data from injured mouse brain	(Hammond et al., 2019)	GEO: GSE121654

Author Manuscript Author Manuscript Author Manuscript Author Manuscript

REAGENT or RESOURCE	SOURCE	IDENTIFIER
Alzheimer's disease, FTD, and PSP exome array data	(Chen et al., 2015)	NIAGADS: https://www.niagads.org/, accession number NG00040
Single nuclear sequencing data from Pick's disease and control precentral gyrus	This study	dbGAP: https://www.ncbi.nlm.nih.gov/projects/gap/cgi-bin/study.cgi?study_id=phs002197.v1.p1
Mouse microglia treated with fatostatin or saracatinib	This study	GEO: GSE146866
5xFAD microglial single cell data	(Keren-Shaul et al., 2017)	GEO: GSE98969
GRCm38	(Dobin et al., 2013)	https://www.ncbi.nlm.nih.gov/assembly/GCF_000001635.20
GencodeM11	(Liao et al., 2019)	https://www.gencodegenes.org/mouse/release_M11.html
Experimental Models: Cell Lines		
1205 (human control) iPSC cell line	Pasca Lab (Stanford)	Obtained from Pasca lab (Stanford)
BV2 (female mouse microglia) cell line	Kind gift from Peter Tontonoz lab; UCLA	RRID: CVCL_0182
Experimental Models: Organisms/Strains		
Primary mouse embryonic cortical neurons from E15 C57BL/6J embryos	Charles River	C57BL/6NCrl
Primary mouse embryonic microglia cultures from P1 C57BL/6J pups	Charles River	C57BL/6NCrl
Software and Algorithms		
Weighted Gene Co-expression Analysis (WGCNA)	(Langfelder and Horvath, 2008)	https://cran.r-project.org/web/packages/WGCNA/index.html
MAGMA v1.06	(de Leeuw et al., 2015)	https://ctg.cncr.nl/software/magma
Broad's CMAP database, version CLUE	(Subramanian et al., 2017)	(https://clue.io)
CQN Package v *1.18.0*	(Hansen et al., 2012)	Source ("http://bioconductor.org/biocLite.R")
STRING for PPI	(Szklarczyk et al., 2017)	https://string-db.org
GOElite Package	(Zambon et al., 2012)	http://www.genmapp.org/go_elite/
Cytoscape v3.4.0	(Saito et al., 2012)	https://cytoscape.org
Transcription Factor Binding Site (TFBS) enrichment analysis	(Chandran et al., 2016)	N/A
NetSig	(Horn et al., 2018)	https://www.lagelab.org/resources/
ImageJ v1.1	N/A	https://imagej.nih.gov/ij/download.html
STAR 2.7.2b	(Dobin et al., 2013)	https://github.com/alexdobin/STAR
RSubread 1.34.6	(Liao et al., 2019)	https://bioconductor.org/packages/3.11/bioc/html/Rsubread.html
ComBat v 1.32.0	(Johnson et al., 2007)	https://rdrr.io/bioc/sva/man/ComBat.html
10X Genomics Cell Ranger (v3.0)	N/A	https://support.10xgenomics.com/single-cell-gene-expression/software/pipelines/latest/installation
Seurat (v3.1)	(Butler et al., 2018)	https://satijalab.org/seurat/install.html